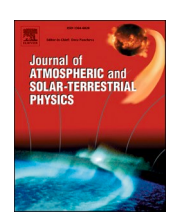
FISEVIER

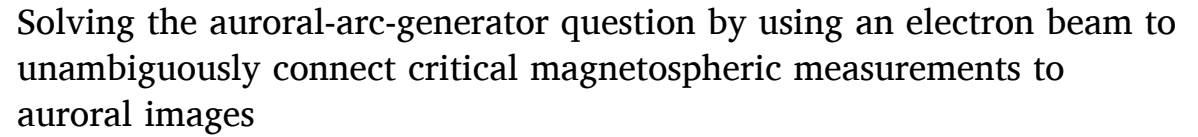
Contents lists available at ScienceDirect

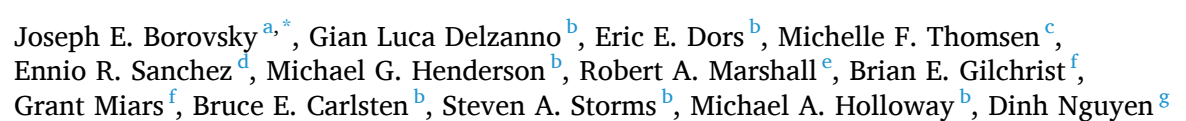
Journal of Atmospheric and Solar-Terrestrial Physics

journal homepage: www.elsevier.com/locate/jastp



Research Paper





- ^a Center for Space Plasma Physics, Space Science Institute, Boulder, CO, USA
- b Los Alamos National Laboratory, Los Alamos, NM, USA
- ^c Planetary Science Institute, Tucson, AZ, USA
- d SRI International, Menlo Park, CA, USA
- ^e University of Colorado, Boulder, CO, USA
- f University of Michigan, Ann Arbor, MI, USA
- g SLAC National Accelerator Laboratory, Menlo Park, CA, USA

ABSTRACT

Keywords:
Aurora
Auroral arcs
Magnetosphere-ionosphere coupling
Plasma physics
Active experiments
Electron beams

ARTICLE INFO

An active mapping mission is described that unambiguously connects measurements in the Earth's magnetosphere to visible aurora in the atmosphere. The core of the mission is an electron-beam source operated on a spacecraft in the equatorial magnetosphere, with the electron beam traveling along the Earth's magnetic-field lines to the atmosphere, depositing its energy to create an optical beam-spot in the atmosphere at the footpoint of the spacecraft's magnetic-field line. This optical spot can be imaged by ground-based cameras, putting the location of the spacecraft's magnetic footpoint into the context of the optical aurora. Scientific instruments carried on the spacecraft make critical measurements of the properties of the magnetosphere at the locations where the magnetosphere powers the aurora, allowing the determination of the plasma-physics mechanisms by which the magnetosphere drives the aurora, in particular answering the outstanding question of how the magnetosphere drives low-latitude auroral arcs. Long-standing questions in magnetosphere-ionosphere coupling that have not been answered because we could not unambiguously connect locations in the magnetosphere with their image in the ionosphere will finally be addressed. In this paper the properties of a "standard" growth-phase auroral arc are collected, theories of the magnetospheric generation of auroral arcs are reviewed, and critical magnetospheric measurements to discern the mechanisms that drive auroral arcs are determined. Further, the plasma physics of the experiment is investigated, including spacecraft-charging mitigation, beam stability, beam scattering, and electron orbit theory. Tradeoffs (keV versus MeV) concerning the energy of the electron beam are enumerated.

1. Introduction

One of the outstanding questions in magnetospheric physics (Denton et al., 2016; Lanchester, 2017; Denton, 2019; Borovsky et al., 2020a) is: what magnetospheric mechanisms produce the aurora in the upper atmosphere? Of the many different types of aurora, how the magnetosphere drives auroral arcs (discrete aurora) is a particularly longstanding and important mystery (Falthammar, 1977; Atkinson,

1978; Swift, 1978; Borovsky, 1993; Paschmann et al., 2002; Haerendel, 2011, 2012): competing theories for the generator mechanisms of quiescent auroral arcs in the equatorial magnetosphere have recently been reviewed by Borovsky et al. (2020b). By generating discrete aurora, the magnetosphere transfers some of its energy to the atmosphere. Because the mechanisms acting to power the aurora arcs are not known, the type of energy extracted from the magnetosphere is not known: it could be thermal energy from ions, thermal energy from

https://doi.org/10.1016/j.jastp.2020.105310

Received 23 February 2020; Received in revised form 27 April 2020; Accepted 4 May 2020 Available online 15 May 2020 1364-6826/© 2020 Published by Elsevier Ltd.



^{*} Corresponding author.

E-mail address: jborovsky@spacescience.org (J.E. Borovsky).

electrons, magnetic energy, flow kinetic energy, Poynting flux of waves in the solar wind, etc. And because the form of energy extraction is not known, the impact of the aurora on the magnetospheric system is not known. Beyond auroral arcs, these same issues pertain to other discrete auroral forms.

Besides the importance of knowing (1) what causes aurora and (2) how aurora impact the magnetospheric system, there has long been a third quest (3) to use auroral observations as a window to observe the global operation of the magnetosphere (Akasofu, 1965; Mende, 2016a, b). To satisfy these desires, the space science community must learn what processes in the magnetosphere create the aurora.

The main reason for the lack of knowledge about how the magnetosphere drives auroral arcs is the lack of mapping knowledge between the magnetosphere and the ionosphere: we have auroral observations and we have spacecraft measurements from the equatorial magnetosphere, but we can't unambiguously connect them together. In the mapping, the important connection between the magnetosphere and the ionosphere is the magnetic-field-line connection: magnetic-field lines guide particle orbits (Feldstein and Galperin, 1993) and magnetic-field lines act as electrical transmission lines guiding current and the Poynting-flux transport of energy (Goertz and Boswell, 1979).

An important example of our poor state of understanding of the magnetosphere-ionosphere connection is the mapping of the observed low-latitude quiescent auroral arc (a.k.a. the "growth-phase arc") into the magnetosphere. Connecting the near-Earth acceleration region of arcs to optical auroral observations has been straightforward (cf. Ono et al., 1987; Stenbaek-Nielsen et al., 1998a,b; Colpitts et al., 2013), but the mapping to the equatorial region where the arc generator operates is ambiguous. One school of thought says the low-latitude arcs magnetically connect into the dipolar portion of the nightside magnetosphere (McIlwain, 1975; Meng et al., 1979; Kremser et al., 1988; Mauk and Meng, 1991; Pulkkinen et al., 1991; Lu et al., 2000; Motoba et al., 2015) while another school believes that the these arcs magnetically connect into the stretched magnetotail (Yahnin et al., 1997, 1999; Birn et al., 2004a,b, 2012; Sergeev et al., 2012; Hsieh and Otto, 2014).

Magnetic mapping between the magnetosphere and the ionosphere is usually done with the use of a magnetic-field model of the magnetosphere (e.g. Tsyganenko and Usmanov, 1982; Tsyganenko, 1989; Tsyganenko and Sitnov, 2007; Sitnov et al., 2008). In these models, as solar-wind and geomagnetic-activity conditions change, the magnetic connection from a point in the nightside ionosphere out into the magnetosphere changes dramatically. Tests of the accuracy of these magnetic-field models in connecting the magnetosphere and ionosphere indicate that the errors are substantial (Thomsen et al., 1996; Weiss et al., 1997; Ober et al., 2000; Shevchenko et al., 2010; Nishimura et al., 2011), too large for the models to be useful for connecting observed auroral arcs with measurements in the magnetosphere. Further, the magnetosphere of the Earth exhibits short-timescale dynamics of the magnetic field are not captured in the parameterized field models.

To overcome these critical mapping issues, a research effort commenced in the 1990's at Los Alamos National Laboratory to develop a technology and a methodology to accurately and unambiguously connect magnetospheric spacecraft measurements to the visible aurora. The solution involves firing an energetic electron beam from a magnetospheric spacecraft, having the Earth's magnetic field guide the beam to the atmosphere, and imaging the optical spot of the beam in the upper atmosphere (Borovsky et al., 1998a; Borovsky, 2002; NASA, 2003, 2006; Delzanno et al., 2016; Borovsky and Delzanno, 2019 Sanchez et al., 2019), while overcoming the technological risks associated with that process (National Research Council, 2012). This paper discusses auroral arcs and current theories for their generation and outlines the mission concept to solve the auroral-arc problem, discussing technological tradeoffs in the experiment design.

This manuscript is organized as follows. In Section 2.1 the properties of low-latitude growth-phase auroral arcs are discussed and the properties of a "standard" auroral arc are collected and in Section 2.2

theories for the magnetospheric generation of auroral arcs are reviewed. In Section 3 the science mission concept to connect magnetospheric spacecraft measurements to aurora in the upper atmosphere is introduced. In Section 4 the tradeoffs between using a keV DC electron gun versus using an MeV radio-frequency accelerator are enumerated. Section 5 outlines the mitigation of beam-driven spacecraft charging. Section 6 studies problems associated with getting the electron beam from the spacecraft to the atmosphere: Section 6.1 deals with locating the direction of the atmospheric loss cone, Section 6.2 discusses beam stability, and Section 6.3 looks at angular scattering of the beam electrons by magnetospheric plasma waves and by field-line curvature. Section 7 overviews the optical detection and location of the beamspot by ground based cameras. Section 8 discusses orbit choices. Section 9 outlines the needed magnetospheric measurements to test the various auroral-arcgenerator theories to determine the mechanisms operating to produce auroral arcs. The manuscript is summarized in Section 10. Additional science topics are enumerated in the Appendix.

2. Auroral-arc properties and auroral-arc generator theories

Auroral arcs in the auroral oval are curtain-shaped east-west aligned regions of optical emission from the upper atmosphere (Lessard et al., 2007; Karlsson et al., 2020). An auroral arc is associated with (1) accelerated energetic (keV) electrons precipitating from the magnetosphere into the atmosphere producing the optical emission, (2) an east-west aligned sheet of upward field-aligned electrical current carried by the precipitating electrons, (3) an inward-pointing electrostatic electric field such that the sheet of the arc is negatively charged, (4) a plasma velocity shear along the arc associated with an $\underline{E} \times \underline{B}$ drift in the electrostatic electric field, and (5) enhanced ionospheric conductivity caused by the impact of the precipitating electrons.

There are three types of quiescent auroral arcs: (1) high-latitude Alfvenic arcs, (2) low-latitude field-line-resonance arcs, and (3) low-latitude growth-phase arcs, where high-latitude and low-latitude refer to locations within the auroral oval. There are also active dynamic arcs during substorms. Quiescent arcs are of most interest here, although the electron-beam experiment will also shed light on the driving of active arcs during substorms.

The high-latitude Alfvenic arcs (Burke et al., 1994; Keiling et al., 2006) are associated with field-aligned current systems in the plasma-sheet boundary layer (PSBL), the boundary between the magnetotail plasma sheet and the lobe. For those arcs the mapping from the arc in the atmosphere into the magnetosphere has little uncertainty, so a spacecraft beam mission is not needed to connect magnetospheric measurements to the atmospheric arc. Field-line-resonance (FLR) arcs (Samson et al., 1996; Gillies et al., 2018) are dim, slowly (minutes) modulated curtains of airglow associated with standing Alfven waves in the dipolar magnetosphere, producing a precipitation of ~100-eV electrons. These FLR arcs, which are not major energy-conversion sites, will not be of concern in this discussion. The focus of the rest of the paper will be on low-latitude growth-phase arcs.

2.1. Properties of low-latitude growth-phase auroral arcs

To guide the discussion and to guide the determination of magnetospheric measurement requirements in Section 9, the properties of a "standard growth-phase arc" are collected into Table 1. This arc is a stable (or very slowly intensifying) arc. The measured parameters of the standard arc are taken from rocket and radar measurements in the literature and those measured parameters are mapped into the magnetosphere where the current-diversion equation (see Section 2.2) applies. The auroral arc is taken to be located in the magnetosphere near geosynchronous orbit (L = 6.6).

The north-south ionospheric thickness of the arc is taken to be $W_{ionos} = 10 \text{ km}$ (e.g. Stenbaek-Nielsen et al., 1998a,b; Knudsen et al., 2001; Dubyagin et al., 2003), although $W_{ionos} = 1 \text{ km}$ (Partamies et al., 2010)

Table 1The "standard" low-latitude growth-phase auroral arc.

		- 2						
Parameter Value Definitison Origin PARAMETERS OF ARC IN THE IONOSPHERE								
	10 km	Arc north-south	Stanback Nielsen et al					
W_{ionos}	10 KIII		Stenbaek-Nielsen et al., (1998); Knudsen et al., (2001)					
	10001	thickness						
L _{ionos}	1000 km	Arc east-west length	Akasofu (1963)					
$j_{ ionos}$	5×10^{-6}	Field-aligned current	Arnoldy (1977); Wu et al.,					
	A/m ²	density	(2017)					
$J_{ ionos}$	50 A/km	Current per length of	Haerendel et al. (2012)					
		arc						
$\Delta \phi$	5000 V	Voltage drop in arc	Marklund (1984)					
ΔB_{ionos}	63 nT	Field shear across arc	Marklund (1984); Bruning and					
		current	Goertz (1986)					
F _{energy} -	25 mW/	Energy flux in	calculated $j_{ } \Delta \phi$					
ionos	m ²	electrons	5111 - T					
Power/km	250 kW/	Power in electron	calculated $j_{ } \Delta \phi W_{ionos}$					
1 OWCI/ KIII	km		calculated J $\Delta \phi$ vvionos					
Darran Arm		precipitation Power in 4278 Å	colordated 1.1 10=3 : A.:					
Power/km	275 W/		calculated 1.1 $ imes$ 10 ⁻³ j $\Delta \phi$					
	km	emission	W _{ionos}					
zenith	5.2 kR	Brightness at 4278 Å	calculated 210 R per 1 mW/m:					
view			Dahlgren et al., (2017)					
zenith	28 kR	Brightness at 5577 Å	calculated 1.2 kR per 1 mW/m:					
view			Steele and McEwen (1990)					
Eionos	50 mV/m	Measured electric	Marklund (1984); Opgenoorth					
		field	et al. (1990)					
V _{shear-ionos}	1000 m/s		Rinnert et al. (1986); Aikio					
			et al. (2002)					
V _{flowthrough}	200 m/s	plasma flow through	Haerendel et al. (1993); Frey					
		arc	et al. (1996)					
PARAMETERS O	F ARC IN EQUA	TORIAL M AGNETOSPHERE						
W_{mag}	330 km	Arc radial thickness	dipole mapping from					
· · mag			ionosphere					
L_{mag}	17000	Arc azimuthal length	dipole mapping from					
⊐mag	km	riic azimadiai iciigai	ionosphere					
4	9×10^{-9}	Field-aligned current	dipole mapping from					
$\dot{\mathbf{J}}_{ }$ mag	A/m^2	density	ionosphere					
т	3×10^{-3}	•	=					
$J_{\mid\mid\ mag}$		Field-aligned current	dipole mapping from					
	A/m	per length	ionosphere					
$\Delta \phi$	5000 V	Perpendicular	mapped from ionosphere					
		Voltage drop						
ΔB_{mag}	3.7 nT	Field shear across	calculated from Ampere's law					
		current sheet						
E_{mag}	15 mV/m	Perpendicular	calculated: $\Delta \phi/W_{mag}$					
		electric field						
v_{shear}	150 km/s	Flow shear with ExB	calculated: E _{mag} x B _{mag}					
$V_{flowthrough}$	6.6 km/s	plasma flow through	dipole mapping from					
		arc	ionosphere					
V _{shear-ionos}	33 km/s	dipole mapping of						
		ionospheric shear						
M AGNETOSPHE	RIC PLASMA PAI							
n	$1~\mathrm{cm}^{-3}$	Number density	Borovsky et al. (1998b)					
T _i	10 keV	Ion temperature	Borovsky et al. (1998b)					
T _e	2 keV	Electron temperature	Denton et al. (2005)					
P _i	1.6 nPa	Ion pressure	calculated: nk _B T _i					
P _e	0.32 nPa	Electron pressure	calculated: nk _B T _e					
В	80 nT	Magnetic field	Borovsky & Denton 2010					
D	50 111	strength	Dolovsky & Deliton 2010					
2	0.00.1	•	11-4-4					
λ_{De}	0.33 km	Electron Debye	calculated					
- (::	5 O I	length	11					
c/ω _{pe}	5.3 km	Electron skin depth	calculated					
c/ω_{pi}	225 km	Ion inertial length	calculated					
r_{ge}	1.3 km	Thermal electron	calculated					
		gyroradius						
r_{gi}	130 km	Thermal proton	calculated					
		gyroradius						
β	0.63	Plasma beta	calculated					
V_A	1800	Alfven speed	calculated					
	km/s							
-								

could also be taken. Growth-phase arcs that are much thicker than 10 km have also been reported (Lessard et al., 2007). The fine-scale (10's of meters) optical structure of arcs (Borovsky et al., 1991; Dahlgren et al., 2008; Sandahl et al., 2011) is ignored. The east-west length of the arc will be taken to be $L_{ionos}=2000$ km (e.g. Fig. 2 of Akasofu, 1963 or Figs. 8 and 9 of Gillies et al. (2014)). The field-aligned current density at the ionosphere is taken to be $j_{||}=5\times10^{-6}$ A/m² (e.g. Arnoldy, 1977;

Marklund et al., 1982; Wu et al., 2017). A current density $j_{\parallel} = 5 \times 10^{-6}$ A/m² for a 10-km wide arc corresponds to a current per east-west length of the arc of $J_{||} = 50$ A/km, or a total current of 100 kA for a 2000-km long arc. The potential drop (accelerating potential) associated with the standard arc is taken to be $\Delta \phi = 5000 \text{ V}$ (Marklund et al., 1982; Marklund, 1984). The shear in the magnetic field across the auroral-arc current sheet is taken to be $\Delta B_{ionos} = 63$ nT (Marklund, 1984; Bruning and Goertz, 1986), consistent with Ampere's law for $J_{\parallel} = 50$ A/km. With the parallel current density $j_{||}$ and the potential drop $\Delta \phi$ the energy flux of electron precipitation onto the atmosphere is calculated to be F_{energy} = 25 mW/m², which corresponds to observations (e.g. Fig. 6e of Marklund et al., 1982). For a 10-km thick arc, the power in electron precipitation is 250 kW/km along the east-west direction. For a 2000-km long arc, this is a total electron precipitation energy of 500 MW, which is about 17% of the ~3 GW of Northern-plus-Southern hemispheric power of "monoenergetic" electron precipitation (cf. Table 1 of Newell et al. (2009)) and which is an even smaller fraction of the 10-20 GW of typical total power in electron precipitation (Emery et al., 2008. 2009). Note that there is a further dissipation of power by the arc associated with the arc's field-aligned current closing as a horizontal current in the resistive ionosphere (e.g. Atkinson, 1978; Haerendel, 2010): this Joule dissipation power can exceed the power in precipitating accelerated electrons (Vickrey et al., 1982). Note also that the arc also has particle- and Joule- power dissipation in the conjugate ionosphere. Using the conversion of 4278 Å emission power being 1.1×10^{-3} of the power in electron precipitation (Bryant et al., 1970), the arc emits a power of 275 W/km in the 4278 Å band. Using the conversion that 1 mW/m² of electron flux is equivalent to a surface brightness of 210 R in the 4278 Å band (Dahlgren et al., 2017), the brightness of the standard arc is 5.2 kR in 4278 Å when viewed edge-on in the magnetic zenith. Using a sky excitation efficiency of 1.2 kR of 5577 Å emission from 1 mW/m² of 3-keV electron precipitation (Steele and McEwen, 1990), the zenith brightness of the standard arc is 28 kR in the 5577 Å line. A north-south velocity of the arc $v_{flowthrough}\, of\, 200\, m/s$ in the ionosphere is taken, based on radar measurements (e.g. Haerendel et al., 1993; Frey et al., 1996), however the presence of such a flow of plasma through the arc is controversial (cf. Williams et al., 1998; Kozlovsky et al., 2001). These values are entered into Table 1.

East-west-aligned low-latitude auroral arcs correspond to approximately azimuthally aligned structures in the nightside equatorial magnetosphere. For a dipole field (which is approximately the case at geosynchronous orbit under modest geomagnetic-activity levels), the geometric north-south compression factor owing to the convergence of magnetic-field lines is about 33:1. Hence, an arc structure that is 10-km thick in the north-south direction in the ionosphere magnetically maps to a structure that is 330-km thick in the radial direction in the equatorial magnetosphere. The east-west/azimuthal compression factor is about 17:1 in the dipole magnetic-field mapping: an arc that is 2000-km long in the ionosphere maps to a structure that is $\sim\!34000~\text{km}=5.4~\text{R}_\text{E}$ long azimuthally in the equatorial magnetosphere. These values are entered into Table 1.

With this magnetic-field mapping, it is straightforward to estimate the magnetospheric parameters of the standard auroral arc. In the equatorial nightside magnetosphere at geosynchronous orbit, B $\sim\!80$ nT (Borovsky and Denton, 2010). Mapping the field-aligned current density $j_{||}$ by keeping $j_{||}/B$ constant results in $j_{||}=9\times10^{-9}$ A/m² in the magnetosphere (by symmetry arguments, the field-aligned current approximately vanishing at the equator). The current sheet in the magnetosphere has a current per azimuthal length of $J_{||}=j_{||}$ Wmag = 3×10^{-3} A/m, which by Ampere's law yields a magnetic shear $\Delta B_{mag}=3.7$ nT across the arc in the magnetosphere (this magnetic shear also approximately vanishing at the equator). The perpendicular potential drop of the arc is the same in the magnetosphere as it is in the acceleration region above the ionosphere: $\Delta \phi=5000$ V. The electric field in the magnetosphere is calculated to be $E_{mag}=\Delta \phi/W_{mag}=15$ mV/m. This magnetospheric electric field yields a shear velocity across the arc

of $v_{shear}=E_{mag}\times B_{mag}=150$ km/s. The north-south velocity of plasma flow through the arc in the ionosphere of $v_{flowthrough}$ maps magnetically to a radial velocity of plasma flow into and through the arc in the magnetosphere of $v_{flowthrough}=6.6$ km/s.

Plasma and magnetic-field measurements at near-midnight geosynchronous orbit yield (cf. Table 1) $n=1~{\rm cm}^{-3}$ (Borovsky et al., 1998b), $T_i=10~{\rm keV}$ (Borovsky et al., 1998b), $T_e=2~{\rm keV}$ (Denton et al., 2005), and B=80~nT (Borovsky and Denton, 2010). In Table 1 the ion pressure is taken to be $P_i=1.6~nPa$ and the electron pressure is taken to be $P_e=0.32~nPa$. These values are entered into Table 1.

With these magnetospheric parameters, standard plasma properties (Debye lengths, skin depths, ion-inertial lengths, gyroradii) are straightforward to calculate (cf. Table 1). Note in Table 1 that the 10-km thickness of the "standard" auroral arc maps to the equatorial magnetosphere to a thickness $W_{mag}=330\ km,$ which is comparable to the local ion inertial length $c/\omega_{pi}=225\ km$ and comparable to the local thermal proton gyrodiameter $2r_{gi}=260\ km$.

If the growth-phase auroral arc magnetically maps into the more-taillike magnetic-field region beyond geosynchronous orbit, then the mapped arc parameters are dependent on the choice of magnetic-field model used for the mapping, and no magnetic-field model contains auroral arcs. Changing the mapping location from quasi-dipolar with an equatorial magnetic-field strength of B = 80 nT to a more-stretched field with B = 27 nT changes the relevant parameters of Table 1 as follows. Accounting for the distortion of magnetic-field mapping from tail-like magnetic geometries to the ionosphere (e.g. Fig. 1 of Kaufmann et al., 1990 or Fig. 22 of Borovsky and Bonnell, 2001), it will be taken that the length of the arc L_{mag} in the magnetosphere stays the same ($L_{mag} \approx$ 17000 km) while the width of the arc in the magnetosphere $W_{mag} \rightarrow$ $3W_{mag} \approx 1000$ km, where the total flux $BL_{mag}W_{mag}$ is conserved in the transformation. Moving outward in the magnetosphere to a weaker-magnetic-field region the plasma number density $n \to n/2 \approx 0.5$ cm-3, $T_i \rightarrow T_i/2 \approx 5$ keV, and $T_e \rightarrow T_i/2 \approx 1$ keV will be taken, which gives $P_i \to P_i/4 \approx 0.4$ nPa and $P_e \to P_e/4 \approx 0.08$ nPa (cf. Borovsky et al., 1998b). Since L_{mag} does not change when the mapping is changed from geosynchronous orbit, v_{shear} does not change so $v_{shear} \approx 150 \ \text{km/s}$ is taken for the further-out mapping. Since $W_{mag} \rightarrow 3W_{mag}$ was taken, $v_{flowthrough} \rightarrow v_{flowthrough}/3 \approx 2.2 \text{ km/s}$ is taken.

2.2. Auroral-arc generator mechanisms

There are a number of theories for the generation of quiescent low-latitude arcs from the nightside magnetosphere (cf. Table 1 of Borovsky (1993) or Table 1 of Borovsky et al. (2020)). Most theories are based on the diversion of perpendicular (to \underline{B}) current into field-aligned current at the site of a perpendicular gradient in the magnetosphere. The

line that the generator mechanism acts. Owing to the B^2 and B^3 denominators on the right-hand side of expression (1), the strongest contribution to $j_{||}/B$ comes from the regions along the field line where the field strength is weakest (near the equator), so taking $L_{||}$ to be half of the distance along a field line from the equator to the Earth will suffice. The first term on the right-hand side of expression (1) represents perpendicular-pressure-gradient driving of parallel currents. The other terms on the right-hand side represent flow braking, vorticity and magnetic-flux change, baroclinic flow $(\nabla T \times \nabla \rho)$, and advected vorticity. Magnetotail computer simulations find that the $\nabla_{\perp}P \times \nabla_{\perp}B$ term tends to be dominant, even in dynamical situations (Birn et al., 1999, 2011). For the pressure-gradient driving of auroral arcs (which have upward field-aligned current coming out of the ionosphere), the vector $\nabla_{\perp}P \times \nabla_{\perp}B$ should be pointing southward in the equatorial plane of the magnetosphere.

The driving of auroral arcs by pressure gradients in the Earth's plasma sheet has been suggested several times (e.g. Stasiewicz, 1985; Galperin et al., 1992; Haerendel, 2007, 2009; Coroniti and Pritchett, 2014). Typically $T_i > T_e$ in the Earth's plasma sheet and so the ion pressure is greater than the electron pressure, hence the focus in the literature has been on ion pressure gradients. Other gradients considered have been density gradients, temperature gradients, and flow gradients (e.g. Roth et al., 1993; Shiokawa et al., 1997; Echim et al., 2007; De Keyser and Echim, 2013). Hybrid arc-generation models have been developed that account for the reaction of the magnetosphere to temporal and spatial variations in ionospheric conductivity (e.g. Sato, 1978; Knudsen, 1996; Watanabe, 2014).

Another way the magnetosphere can drive field-aligned currents is via the diversion of Hall currents in a thinned, cross-tail current sheet (Schindler and Birn, 2002; Birn et al., 2012; Yang et al., 2013; Hsieh and Otto, 2014). Whereas the gradient mechanisms (cf. expression (1)) can operate in the dipolar and stretched-dipolar portions of the nightside magnetosphere, the thin-cross-tail current-sheet mechanism operates in the stretched magnetotail and the transition region from the stretched magnetotail to dipole field lines. When a current sheet thins to scales sizes of ion gyroradii and below, the equations of motion of ions and electrons differ and flows associated with $\underline{E} \times \underline{B}$ drift become Hall currents as the electrons $\underline{E} \times \underline{B}$ drift but the ions do not. The thin current sheets also gain a net negative space charge, producing an arc-like electrostatic electric field that maps from the magnetotail current sheet along magnetic-field lines toward the ionosphere.

Focusing on growth-phase auroral arcs, this experiment is designed to answer the questions of what mechanisms provide the power for the arcs, what mechanisms divert the current from the magnetosphere, and what mechanisms produce the perpendicular electric fields and related E-cross-B flows.

$$\left(1 \left/ L_{||}\right) \left(j_{||} \middle/ B\right) = \left(2 \middle/ B^{3}\right) \left(\left(\nabla P_{i} + \nabla P_{e}\right) \times \nabla B\right)_{||} + \left(2\rho \middle/ B^{3}\right) \left(\left(dv/dt\right) \times \nabla B\right)_{||} - \left(1 \middle/ B^{2}\right) \left(\left(dv/dt\right) \times \nabla \rho\right)_{||} + \left(\rho \middle/ B^{3}\right) \omega \cdot d\mathbf{B} \middle/ dt + \left(\omega_{||} \middle/ eB^{3}\right) \left(\nabla k_{B}T \times \nabla \rho\right)_{||} + \left(\rho \middle/ B^{2}\right) d\omega_{||} \middle/ dt$$

$$(1)$$

field-aligned current j_{\parallel} resulting from current diversion is described by a generalization of the "Vasyliunas formula" (Grad, 1964; Vasyliunas, 1970)

(e.g. eq. (3.21) of Schindler and Birn (1978), eq. (5) of Sato and Iijima (1979), eq. (15) of Hasegawa and Sato (1979), and eq. (12) of Strangeway (2012)) where B is the magnetic-field strength, P_i and P_e are the ion and electron pressure, ρ is the plasma mass density, \underline{v} is the plasma flow velocity, and $\omega = \nabla \times \underline{v}$ is the vorticity. $L_{||}$ on the left-hand side is the length away from the equator along a magnetospheric field

3. Science mission concept

The concept of the mission (cf. Fig. 1) is an electron beam source mounted on a spacecraft in the equatorial region of the magnetosphere with an orbit with a 24-hr period. Through each 24-hr interval the spacecraft's magnetic footpoint in the upper atmosphere will wander across an array of ground based optical cameras in the auroral zone. The firing of the electron beam into the atmospheric loss cone will deposit energy in the atmosphere, producing an optical spot marking the location of the spacecraft's magnetic connection to the atmosphere in the context of auroral images. The spacecraft will carry scientific

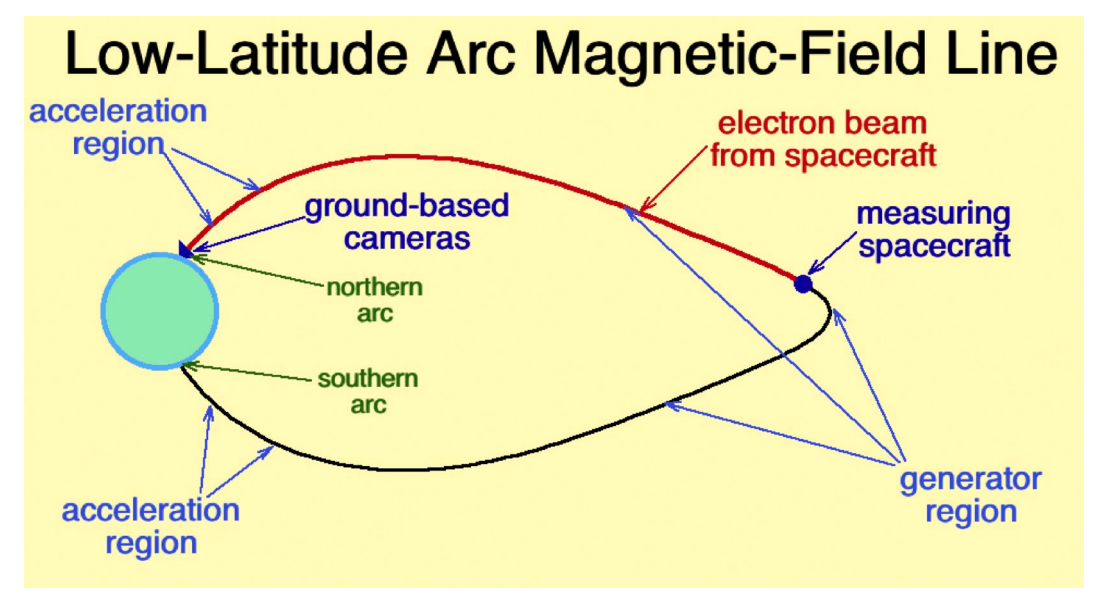


Fig. 1. A sketch of the magnetospheric spacecraft in the auroral generation region of the magnetosphere sending an electron beam along the magnetic field line into the aurora in the atmosphere. In the atmosphere, an optical beam-spot at the magnetic "footpoint" of the spacecraft is located via a network of ground-based optical cameras.

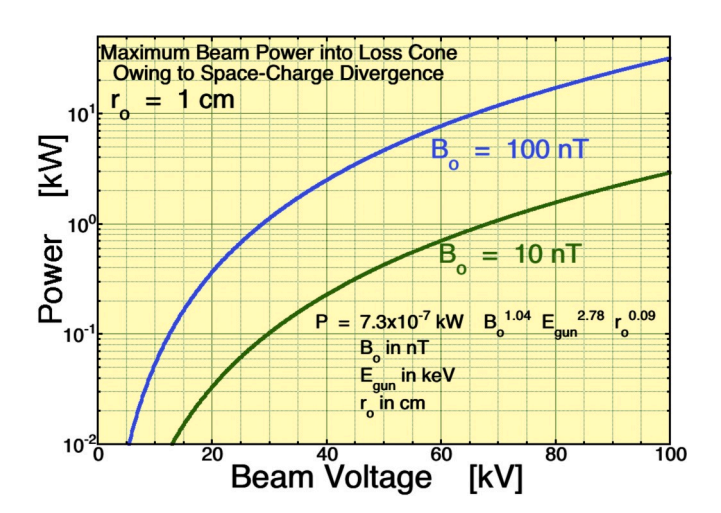


Fig. 2. A plot of the maximum power that an electron beam can deliver to the atmosphere from the geosynchronous-orbit equator versus the beam voltage. The calculation is based on matching the amount of space-charge expansion of the electron beam after it leaves the electron gun with the angular size of the atmospheric loss cone. The empirical expression for the maximum power is shown in the figure.

instrumentation to measure the properties of the magnetosphere sufficient to determine the physical mechanisms that drive the various types of aurora, in particular auroral arcs. Note (as depicted) that the generation region for the auroral arc extends for a significant distance away from the equator (minimum-magnetic-field location).

The operation of the electron accelerator involves the accelerator, a power-storage system, a plasma contactor, and a scientific magnetometer. To create an optical beam spot in the upper atmosphere that marks the magnetic footpoint of the spacecraft, the electron beam must be fired into the atmospheric loss cone: for low-energy (keV) electrons the center of the loss cone is aligned with the local magnetic-field direction, but for higher-energy (MeV) electrons the atmospheric loss cone is displaced eastward of the magnetic-field direction (as discussed in Section 6.1). Tradeoffs between low-energy (keV) electron guns and higher-energy (MeV) electron accelerators are discussed in Section 4. The magnetometer provides information about the exact direction of the ambient

magnetic field prior to the beam firing.

With a 1–100 mA electron beam fired for 0.5 s, 5×10^{-4} - 5×10^{-2} C of negative charge is removed from the ungrounded spacecraft in the tenuous magnetosphere. Without technical intervention, catastrophic spacecraft charging would occur. A plasma contactor on the spacecraft will be initiated prior to the accelerator operation with the ion and electron currents of the contactor exceeding the electron emission of the accelerator (cf. Prech et al., 1995, 2018). Extensive theoretical analysis and computer simulations of the beam and contactor in the magnetosphere has led to a new picture of how the contactor will eliminate spacecraft charging (Delzanno et al., 2015a, 2015b; Lucco Castello et al., 2018): rather than the contactor's Xenon-plasma plume acting as a collector of magnetospheric electrons to ensure current balance, the contactor's plasma plume will act as an emitter of Xenon ions to ensure current balance. Laboratory experiments have been performed to verify the simulation results (Miars et al., 2016, 2017, 2018a; b, 2020). Spacecraft-charging mitigation will be discussed in detail in Section 5.

An orbit for the magnetospheric spacecraft can be selected to cross through the equatorial magnetospheric regions that are believed to be the generator regions of various types of discrete aurora while the Northern-Hemisphere atmospheric magnetic footpoint of the spacecraft passes over a North American ground-based camera array. The types of discrete aurora thus intercepted by the spacecraft will include lowlatitude quiescent arcs (a.k.a. growth-phase arcs) (Lessard et al., 2007), high-latitude quiescent arcs (Safargaleev et al., 2003), active auroral arcs (a.k.a. breakup arcs, substorm arcs) (Goertz, 1985), auroral streamers (Henderson et al., 1998), omega bands (Henderson, 2012), black aurora (Trondsen and Cogger, 1997), giant undulations (Henderson et al., 2010), etc. The spacecraft will also intercept the magnetospheric region of pulsating aurora, which are diffuse aurora with discrete spatial features (Partamies et al., 2019; Nishimura et al., 2020). To optimize the nighttime conjunction time of the spacecraft's magnetic footpoint with the camera array, orbits with periods of 24 h are explored in Section 8.

Detection of the beam-spot in the atmosphere and monitoring of the aurora can be made via an array of optical all-sky cameras covering a significant portion of Canada (Spanswick et al., 2018). The energy deposition of the electron beam in the atmosphere will produce a magnetic-field-aligned cylinder of optical emission from de-excitation of excited N_2^\pm radicals created by the impact of beam electrons ionizing air

molecules (Davidson and O'Neil, 1964; Marshall et al., 2014, 2019). A tens of keV electron gun will deposit its beam energy at an altitude of ~100 km; a 1-MeV accelerator will deposit its beam energy at an altitude of about 60 km; lower-energy (~keV) auroral electrons deposit their energy at an altitude of about 130 km (Rees, 1963; Boyd et al., 1971). An on-off-on firing sequence will be chosen for the accelerator operation to produce an on-off-on blink sequence for the optical beam-spot, making the beam-spot easier to locate in the presence of optical aurora. Software must be implemented to translate the cylindrical beam-spot up along the magnetic-field direction into the context of the aurora in the camera images. Beam-spot detection will be discussed in detail in Section 7.

As the spacecraft crosses through auroral generation regions in the magnetosphere (and simultaneously the beam-spot at the magnetic footpoint crosses through auroral forms in the atmosphere), measurements should be continuously taken that are relevant to present-day theories of auroral generation. For stable quiescent auroral arcs, the various theories (cf. Section 2 and see also Borovsky et al., 2020) focus on ion pressure gradients, electron pressure gradients, magnetic-fieldstrength gradients, flow shears (vorticity), thin-current-sheet formation, Alfven waves, particle-anisotropy boundaries, plasma density gradients, and flow braking. Theories of active discrete aurora involve flow shears, flow braking, pressure gradients, and Alfven waves. To cover these important auroral-generation processes, the spacecraft in the magnetosphere should measure the magnetic-field vector, the ion flow vector, the electron flow vector (i.e. the electric field), the ion pressure, the electron pressure, the ion and electron anisotropies, and the hot-plasma density. Measurement requirements to solve the question of how auroral arcs are driven are discussed in Section 9.

4. A 10's-of-keV electron gun versus an MeV electron accelerator

The technology of operating high-power electron beams in space has been verified: electron guns with powers of 30 kW (O'Neil et al., 1978) and 40 kW (McNutt et al., 1995) have been operated, beams with currents of up to 18 A have been flown (Rappaport et al, 1993) and gun voltages of up to 45 kV (Winckler et al., 1975) have been flown. A 1-MeV radio-frequency proton accelerator has flown in space (Nunz, 1990; O'Shea et al., 1991; Pongratz, 2018) and a design is being prototyped for a spaceflight-qualified 1-MeV radio-frequency electron linac (Lewellen et al., 2019) and the technology of that prototype will be tested on an upcoming rocket flight (Reeves et al., 2020).

In deciding whether to use a tens-of-keV electron beam created with a DC electron gun or an MeV electron beam created with a radio-frequency electron accelerator, there are a number of tradeoffs to consider. Some of these are listed in Table 2.

A major consideration is spacecraft charging when the electron beam

Table 2 Tradeoffs between a ~40-keV electron gun and a ~1-MeV electron accelerator.

Tradeoff	keV	MeV
1. Spacecraft charging		better
Beam divergence versus size of loss cone		better
3. Knowing where the loss cone is located	better	
4. Spot altitude and quenching	better	
5. Radar energy deposition: height, beam temporal sequence	better	
6. Long-distance stability of propagating beam		
7. Operation in presence of contactor plasma and gas		
8. Pointing accuracy		
9. Ease and angular range of beam steering	better	
10. Efficiency: energy storage to beam power		
11. Mass of accelerator and storage system		
12. Thermal issues		
13. Launch vibration issues		
14. Interference: magnetic, radio-frequency,		
15. Spaceflight heritage and risk:		
Power storage, power conversion, accelerator, steering, control		

removes negative charge from the ungrounded magnetospheric spacecraft (Spacecraft charging is analyzed in Section 5.). The amount of charge Q that is removed during a beampulse is given by $Q=I\Delta t$ where I is the beam current and Δt is the beampulse duration. The power P of the beam is P=IV where V is the beam Voltage (beam energy). MeV beams have the great advantage over keV beams because they can deliver the same power P with much less current I, and hence will remove much less charge Q from the spacecraft, lowering the severity of the spacecraft-charging problem.

A second important issue is related to beam angular divergence, the angular size of the atmospheric loss cone, and the amount of beam power that can be injected into the loss cone. The space charge per unit length Q/L of an electron beam is given by Q/L = I/v where v is the beam speed. A keV beam has a much larger value of Q/L than an MeV beam since the keV beam needs more current I to carry the power and has a lower beam speed v. Space charge causes the beam to expand electrostatically in the transverse direction, with the beam electrons picking up transverse velocity in the expansion. This gives the electron beam an angular spread as it propagates away from the spacecraft. For keV-range beams the maximum beam current that can be put into the loss cone (translated as a maximum beam power into the loss cone) is plotted in Fig. 2. The formula (derived in Borovsky (2002))

$$P = 7.3 \times 10^{-7} \ kW \ (B_o/1 \ nT)^{1.04} \ (E_{gun}/1 \ keV)^{2.78} \ (r_o/1 \ cm)^{0.09} \eqno(2)$$

is used, where B_{o} is the magnetic-field strength at the spacecraft, E_{gun} is the energy of the beam (beam Voltage), and ro is the radius of the beam at the exit of the gun. To get more electron-beam power into the loss cone, higher Egun is better, larger Bo is better, and a larger initial beam radius r₀ is better. There are multiple physical processes going into the scalings of expression (2). Higher values of Egun are better for three reasons: (1) higher Egun mean lower beam space charge which reduces the transverse electrostatic expansion of the beam and reduces the pitch angles of the beam electrons so they more-easily fit into the loss cone, (2) a higher value of E_{gun} means for a given $v\perp$ the beam-electron pitch angle will again have a lower pitch angle, and (3) holding everything else fixed a larger E_{gun} represents more beam power. Higher values of B_o are better for two reasons: (1) the loss cone is larger when B₀ is bigger and (2) the electrostatic transverse expansion of the electron beam ceases when a $\textbf{v}_{\perp} \times \textbf{B}_{0}$ force overcomes the electrostatic force and this occurs in one quarter of a cyclotron period which is πγmec/2eB_o. Larger values of the initial beam radius ro are better because the beam transverse electric field is weaker for a larger beam radius, meaning there is reduced transverse expansion leading to v_{\perp} . The blue curve in Fig. 2 is for a field strength of $B_{o}=100\ nT$ at the spacecraft (a 2.56° loss cone) and the green curve is for $B_{0}=10\ nT$ (a 0.91° loss cone). As can be seen in Fig. 2, power into the loss cone can be severely limited for electron guns that operate at less than several 10's of keV. Beams with energies of less than 10's of keV would also suffer perturbations from spacecraft charging and from auroral potentials between the magnetosphere and the ionosphere.

A third issue in Table 2 is the ability to locate the direction of the atmospheric loss cone. An onboard magnetometer must be used to determine the instantaneous direction of the magnetospheric magnetic fields at the location of the spacecraft prior to beam firing. The issue is that the center of the loss cone shifts away (in the eastward direction) from the direction of the magnetic field for higher-energy electrons (This is analyzed in Section 6.1.). For dipolar magnetic-field lines the magnitude of the angular shift can be predicted; for non-dipolar (stretched) field lines this prediction might not be possible and trial and error beam firings might be needed to find a firing direction that results in an atmospheric beam spot.

Items 4 and 5 in Table 2 deal with the altitude of the beam spot in the atmosphere (\sim 60 km for 1 MeV and \sim 100 km for 10's of keV). At the lower altitude of the MeV beamspot the atmosphere is more dense and

collisional quenching of the beamspot optical emission acts to make the beam power less efficient (analyzed in Section 7); for the 10's-of-keV beamspot collisional quenching is not an issue. If one wanted to study the ionization beamspot via ground-based radar (e.g. Izhovkina et al., 1980; Uspensky et al., 1980; Zhulin et al., 1980), the denser atmosphere for the MeV beam results in rapid electron attachment removing the free electrons that produce radar backscatter, making radar imaging difficult (analyzed in Section 7); this is a much reduced problem for the keV beamspot altitudes.

Items 6 and 7 in Table 2 concern the stability of the electron beam as it propagates through the magnetospheric plasma (and perhaps through the much-denser contactor plume plasma) and concern the angular scattering of the beam electrons by naturally occurring ambient magnetospheric plasma waves. Few-MeV relativistic-electron beams behave differently than 10's-of-keV nonrelativistic-electron beams do. This trade study is discussed in Section 6.2; no answer as to advantages and disadvantages of MeV versus 10's of keV on these issues has been attained yet.

Items 8–16 in Table 2 concern the practicality of the design and operation of the electron beam source (gun versus accelerator), its power efficiency, the needed energy-storage systems, thermal issues (e. g. an RF accelerator becoming de-tuned owing to thermal expansion), and launch vibration issues. Two great concerns are (11) the total mass of the accelerator and energy-storage system and (15) the pathway to low-risk spaceflight heritage.

5. Spacecraft charging mitigation

Although using electron beams to trace magnetic field lines is a several-decades-old idea, it has never been realized in practice because of fear of catastrophic spacecraft charging that could be induced by a high-power electron beam in the low-density environment of the magnetosphere. A call had been made in the most-recent National Academies decadal survey to solve this problem (National Research Council, 2012). In order to get an estimate of the problem, we can consider a characteristic space environment at geosynchronous orbit with plasma density $n = 1 \text{ cm}^{-3}$, electron temperature $T_e = 1 \text{ keV}$, and ion temperature $T_i = 10$ keV. As the beam is fired, the spacecraft charges positively and collects plasma from the background until a dynamic equilibrium is established where the sum of all currents (collected and emitted) on the spacecraft is zero. Such equilibrium can be calculated analytically within the orbital-motion-limited (OML) collection theory for a spherical probe (Mott-Smith and Langmuir, 1926), which is a reasonable approximation since for these parameters the characteristic plasma scales such as the electron Debye length or the electron gyro-radius are much larger that the size of the spacecraft. A 1-kW beam power can be obtained with beam energy E = 10 keV and current I_B = 100 mA or with beam energy E=1 MeV and $I_B=1$ mA. For the 10-keVcase, OML gives an equilibrium spacecraft potential equal to 10 MV. Since this value is higher than the beam energy, the beam would not be able to escape the electrostatic attraction of the spacecraft and would quickly be pulled back to the spacecraft. For the 1-MeV case, the OML spacecraft potential is 100 kV. This value is lower than the beam energy, implying that the beam would be able to propagate away from the spacecraft, but still unacceptably large from the perspective of safe spacecraft operation. Going to higher beam energy and lower beam current would help the spacecraft-charging scenario, but is problematic because of issues of knowing where the loss cone is located that are discussed in Section 6.1. This simple exercise underlines two important conclusions: the ability to lower the beam current by increasing the beam energy is important to reduce spacecraft-charging problems but still insufficient to resolve them completely, and, consequently, a spacecraft-charging mitigation scheme is necessary.

To neutralize the charged removed from the magnetospheric spacecraft by the electron beam, one might consider simultaneously emitting a positive-ion beam of equal current. This concept, however,

fails owing to the severe Child-Langmuir space-charge limit for ion emission (Delzanno et al., 2015b; Child, 1911; Langmuir and Blodget, 1924). The low velocity of current-carrying ions (in comparison with electrons) results in the build up of a high density of space charge at the emission point of the ion beam, creating a positive potential that inhibits the ion beam from exiting the ion gun.

In terms of spacecraft-charging mitigation, the plasma-contactor technology has been successfully used in several past missions (Olsen, 1985; Gilchrist et al., 1990; Katz et al., 1994; Prech et al., 1995; Comfort et al., 1998). The concept is based on the emission of a high-density, charge-neutral plasma prior to and during beam emission. The contactor plasma plume is thought to make contact with the background plasma (hence the name 'contactor'), in which case it acts effectively as a way to increase the collection area of the spacecraft with respect to the background electrons. Particle-In-Cell (PIC) simulations were performed to study the beam-contactor-spacecraft interaction both in vacuum and in the presence of a background plasma (Delzanno et al., 2015a,b). These simulations are challenging because of the large scale separation that needs to be resolved in the system, from the small Debye length (~cm) at the contactor injection to the large scale (ideally ~ km) of the contactor plume, and could be performed only for the early time of an actual space experiment. Nevertheless, they showed that the contactor would not work as an electron collector in the tenuous magnetospheric plasma but could work very effectively for the emission of ions. This is because the quasi-spherical contactor plume lowers the space-charge limits that normally reduce the emission of ions (and that, in general, would prevent compensating the electron beam with an equal-current ion beam) and hence allows the emission of substantial ion currents (Delzanno et al., 2015a,b).

In order to obtain quick estimates of the long-time spacecraft charging during beam emission, a reduced model has been developed by Lucco Castello et al. (2018). The initial condition of the contactor plume prior to beam emission is the input for the model, which is spherically symmetric and valid in the limit where the contactor ion current and the beam current are equal. In this case, the contactor electrons only provide a quasi-static electron population around the spacecraft, where electron and ion densities are approximately equal (i.e. a quasi-neutral region). The contactor ions can flow from the quasi-neutral region, creating an ion-rich region where ions are pushed away from the spacecraft by the positive charge left behind by the electron beam. The main result of

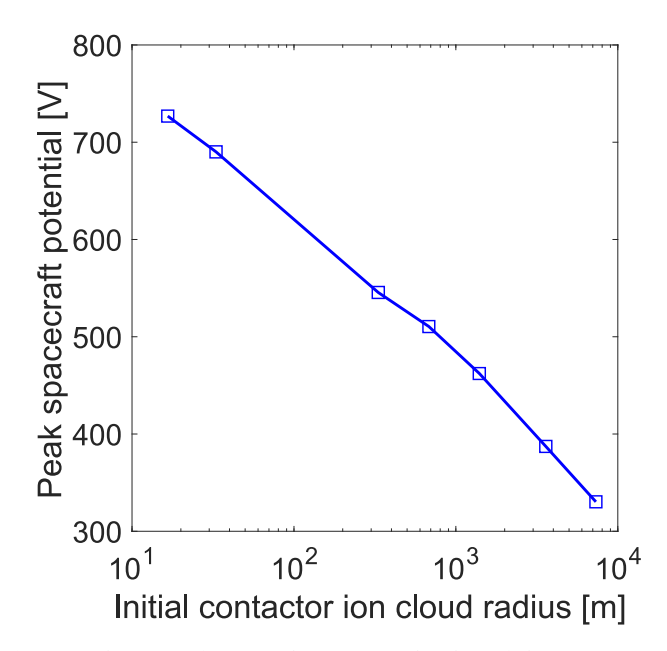


Fig. 3. Peak spacecraft potential versus initial radius of the ion contactor plume prior to the emission of a 1-mA electron beam for 0.5 s.

Lucco Castello et al. (2018), supported by comparisons with PIC simulations, is that only the dynamics of the outermost surface of the quasi-neutral and ion-rich regions controls the transient of the spacecraft potential and that this is essentially governed by space-charge (Child-Langmuir) physics. Furthermore, the bigger the initial ion contactor plume before beam emission, the lower the peak of the spacecraft potential. Fig. 3 shows predictions using the reduced model for a series of simulations where a Helium contactor was released for 0.3, 0.6, 5, 10, 20, 50, and 100 ms, respectively, prior to firing a 1-mA electron beam for 0.5 s. Fig. 3 shows the initial maximum radius of the ion-rich contactor region versus the maximum spacecraft potential obtained by the model (Colandrea, 2018). The peak spacecraft potential is on the order of several hundred volts. A Helium contactor gas has been used for ease of the PIC simulations, but the scaling law of peak spacecraft potential φ_{sc-max} versus contactor ion mass m_i, which was derived in (Delzanno et al., 2015a; Lucco Castello et al., 2018) as

$$\varphi_{\text{sc-max}} \propto \text{mi}1/3$$
 (3)

indicates that the peak spacecraft potential for an Argon or Xenon contactor would only be a factor of two-three higher than what obtained for Helium. Another factor of order unity (quantified in $\sim\!1.7$ by some of our preliminary simulation work) is necessary to account for the fact that the contactor expansion is not exactly spherically symmetric. All together, these results show that the peak spacecraft potential in a magnetospheric experiment would be of the order of a few kV or lower. This is significantly lower than the beam energy, implying that an electron beam can be easily emitted by the spacecraft. Furthermore, longer contactor expansion times prior to beam emission can limit the peak spacecraft potential to less than 1 kV. Note also that kV potentials on magnetospheric spacecraft are common (Thomsen et al., 2013) and do not normally present a threat for spacecraft, provided that the spacecraft platform is designed to avoid differential charging and the threat of electrostatic discharges.

In order to validate the theoretical and simulation work on contactor-based spacecraft-charging mitigation, laboratory experiments have been conducted at the University of Michigan Plasmadynamics and Electric Propulsion Laboratory (PEPL). In these experiments, an electrically isolated hollow cathode represents the electron-beam spacecraft. This hollow cathode emits a quasi-neutral plasma while electron beam emission is mimicked through a separate, constant-current power supply. Plasma diagnostics mounted on various moving stages in the vacuum chamber were added to this base configuration to measure quantities which validate specific aspects of the theoretical framework. Specifically, parameters predicted to dominate ion emission include plasma potential, plasma geometry, and ion drift velocity (Lucco Castello et al., 2018). These parameters were measured at specific positions near the vacuum-chamber walls using emissive probes and a Retarding Potential Analyzer (RPA) (Miars et al., 2018b). The actual current emitted at these positions was also measured for comparison using 10-cm² planar probes (Miars et al., 2018b). This set of experiments was repeated for a large chamber (8 probe positions) and small chamber (7 probe positions) to vary the plasma geometry in a controlled manner and obtain a large sample size for more rigorous validation. The analyses of these vacuum-chamber experiments (Miars et al., 2020) have provided quantitative confirmation of the space-charge-limited nature of ion emission predicted by PIC simulations and the reduced model (Delzanno et al., 2015a, 2015b; Lucco Castello et al., 2018; Miars et al., 2018b).

6. Getting the beam to the atmosphere

To maximize the fraction of the electron beam entering the atmosphere, the beam must be injected into a geometrical region known as the atmospheric loss cone and must propagate far enough to reach the atmosphere. Beams with energies of up to 40 kV were propagated long distances through the magnetosphere in the Echo series of experiments (Hallinan et al., 1990; Winckler, 1992) and electron beams of 27 kV, 0.5

Amp and 15 kV, 0.5 Amp on the two ARAKS experiments were propagated $8.2~R_E$ through the magnetosphere without disruption (Pellat and Sagdeev, 1980; Lavergnat, 1982).

Three issues are discussed: (1) locating the loss cone, (2) beam stability, and (3) scattering of the beam electrons by ambient magnetospheric plasma waves and by field-line curvature. Ballistic particle calculations, consideration of beam-plasma instabilities, and consideration of scattering by ambient plasma waves all indicate that the electron beam will propagate from the magnetosphere to the atmosphere to deposit its energy. The ballistic particle simulations also provide the initial conditions for calculations of the optical signature of the beam in the atmosphere.

6.1. Locating the loss cone

It is optimal to put 100% of the beam energy into the loss cone. Standard calculation of the loss cone involves the conservation of the first adiabatic invariant of each beam electron (e.g., Rossi and Olbert, 1970). For low-energy particles with small gyroradii, the calculation of the position of the loss cone is sufficiently accurate using the zeroth-order term $\mu^{(0)} = v \perp^2 / B$ of the first adiabatic invariant expanded in the small parameter r_c/L_B (Northrop, 1963; Gardner, 1966) where r_c is the particle gyroradius and L_B is a gradient scale of the magnetic field. For small-gyroradii particles the circular loss cone has its center in the direction of the local magnetic-field vector, i.e. the center of the loss cone corresponds to a pitch angle of 0°. For more-energetic electrons the center of the loss cone shifts eastward from the magnetic-field direction. Porazik et al. (2014) explored the fact that higher-order terms of the magnetic-moment expansion can more-correctly determine the location of the loss cone (see also Mozer (1966) and Il'ina et al. (1993)). Fig. 4 (middle) shows the equatorial pitch angles (δ) of energetic electrons that would lead to atmospheric precipitation for different azimuthal injection angles (λ) as a function of electron energy at 10 R_E in a dipole magnetic field. For comparison, the dashed line shows the loss cone computed based on only the lowest-order term $\mu^{(0)}$ of the magnetic-moment expansion. The importance of higher-order terms is most dramatically reflected in the $\lambda\text{-dependence}$ of the loss cone. Note that the shift of the loss cone is in the $\lambda = -90^{\circ}$ direction: examining the left panel of Fig. 4 one sees that the λ $=-90^{\circ}$ is eastward. As the energy of the electron increases, the loss-cone shift becomes larger, and eventually the loss cone becomes a closed contour in the δ - λ plot with unique boundaries in both angles, as Fig. 4 (right) shows.

In a dipole magnetic-field geometry at the equator, the loss cone remains circular and the center of the actual atmospheric loss cone is shifted away from the magnetic-field direction into the curvature-drift direction by an angle $\Delta\theta$ given by Eq. (4) of Mozer (1966) as

$$\Delta\theta = Arcsin(v_c/v_o) \tag{4}$$

(the "Mozer transform"), where v_c is the equatorial value of the curvature drift and v₀ is the speed of a beam particle. At the equator of the Earth's dipole magnetic field, the curvature drift for an electron is given by $v_c = 3\gamma m_e cv_1^2/eB^2r$ (cf. Eq. (5.32) of Spjeldvik and Rothwell (1985)), where γ is the relativistic factor, m_e is the electron mass, c is the speed of light, $v_{||}$ is the electron speed along the magnetic field, e is the electron charge, B the field strength, and r the distance from the center of the Earth. For electrons, as seen in Fig. 4 (left), the loss cone shifts in the eastward direction from the magnetic field direction. In the Mozer-transformed reference frame, a good approximation of the first adiabatic invariant is $\mu = |v_{\perp} - v_c|^2/B$ rather than $\mu = v_{\perp}^2/B$ (cf. Eq. (4) of Mozer (1966)). In Fig. 5 the angular shift eastward of the atmospheric loss cone from the direction of \underline{B} (pitch angle 0°) is plotted in red for a 1-MeV electron beam for the accelerator at the dipole equator. Also plotted (blue curve) is the approximate angular radius of the loss cone as seen from the equator. In dipolar fields out to 12 RE, the angular shift of the loss cone is substantially less than the angular size of the loss cone

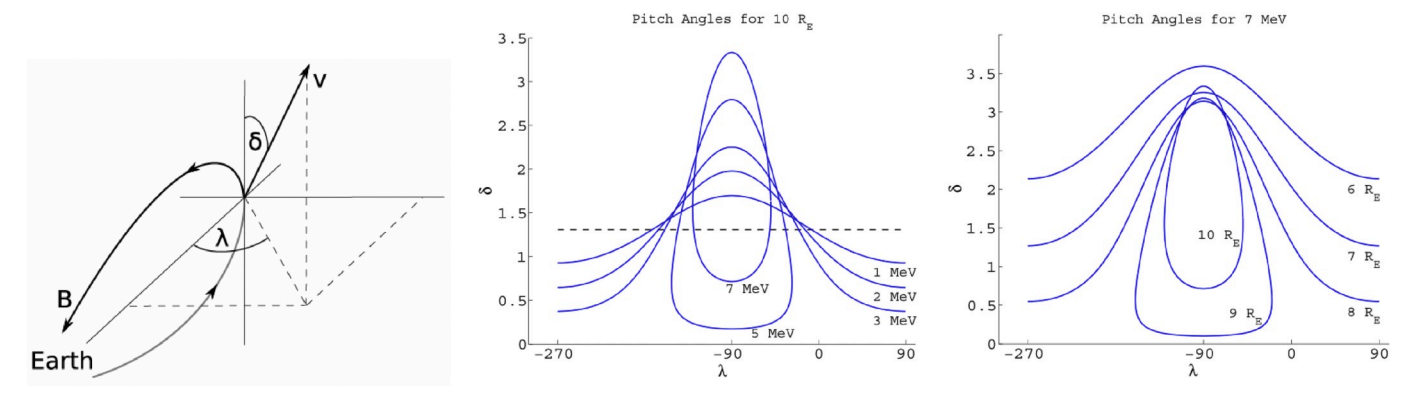


Fig. 4. Geometry for injection of beam MeV electrons (left). The angle δ is the traditional pitch angle, the azimuth λ denotes the angle away from the plane of the flux surface. Edges of loss cones for an electron initialized from 10 R_E at the equatorial plane of a dipole field for different energies (middle) and for a 7-MeV electron initialized from different distances at the equatorial plane of a dipole field (right). The black dashed line corresponds to the unmodified loss cone for injection from the equatorial plane. After Porazik et al. (2014).

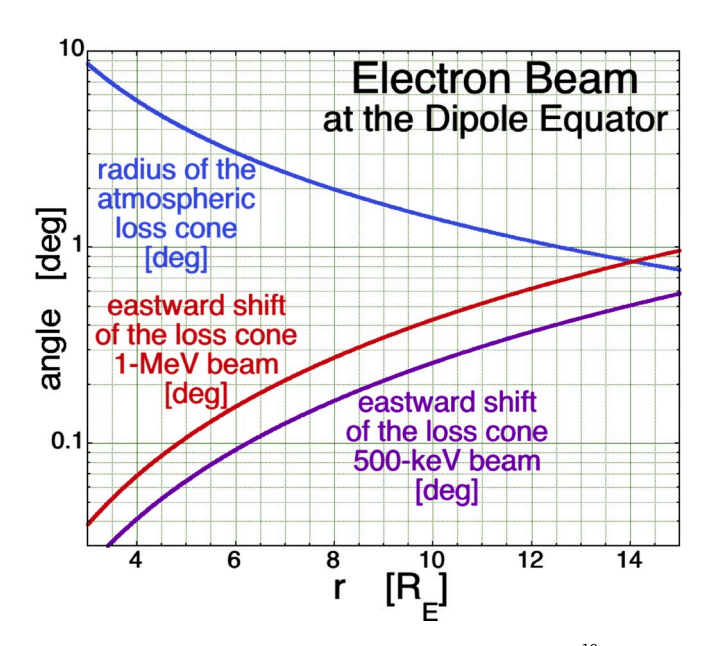


Fig. 5. For a 1-MeV electron beam ($\gamma=2.96,\ v_{||}=2.83\times 10^{10}\ cm/s$) the eastward shift of the loss cone owing to the curvature drift (Mozer, 1966) is plotted as the red curve for the accelerator operated in the Earth's dipole equator. The purple curve is the shift when the accelerator is operated at only 500-keV ($\gamma=1.98,\ v_{||}=2.58\times 10^{10}\ cm/s$). The blue curve is the approximate angular radius of the loss cone. (For interpretation of the references to color in this figure legend, the reader is referred to the Web version of this article.)

and so without even correcting for the Mozer transform a beam with a small angular divergence will hit the atmosphere. However, beyond r $\sim\!6$ R_E the nightside magnetic field can be non-dipolar. For a non-dipole field, the angular shift of the loss cone is larger than for a dipole ((Willard et al., 2019a) and the shift is not predictable because the radius of curvature of the magnetic field is not known and so the curvature-drift velocity vector v_c is not calculable.

6.2. Beam stability

One area of ongoing research is the determination of the stability properties of the electron beam as it travels along the magnetic-field line through the magnetospheric plasma to the topside atmosphere. Simple linear analysis suggests that the electron beam propagating through the magnetosphere will be unstable to electrostatic two-stream instabilities but this will not be a problem because the instability growth rates are

very small relative to the propagation time of the beam (Galvez and Borovsky, 1988). Furthermore, the beam propagating into the ionosphere will be stable to resistive hose, ion hose, and filamentation instabilities (Gilchrist et al., 2001; Neubert and Gilchrist, 2002, 2004). Simulations that track the beam from its source in the magnetosphere to its contact with the topside atmosphere are currently being carried out to quantify the effects of beam-plasma interaction as the beam moves through magnetic field and plasma-density gradients. Initial particle-in-cell simulation results, supported by theoretical analysis, suggest no major effect of instabilities on the beam propagation (Kaganovich, private communication). Simulation results will be reserved for a future publication.

6.3. Scattering by magnetospheric plasma waves and by field-line curvature

To get the beam electrons into the atmosphere one must also consider pitch-angle scattering of the beam electrons by ambient magnetospheric plasma waves.

For 1-MeV beam electrons (radiation-belt energies) the waves to worry about are electromagnetic ion-cyclotron (EMIC) waves and whistler-mode chorus waves. In the plasma sheet away from the plasmasphere the amplitude of EMIC waves is low (cf. Fig. 8 of Anderson et al. (1992), Fig. 7 of Clausen et al. (2011), and Figs. 3 and 8 of Usanova et al. (2012)). In the nightside magnetosphere at 7 R_E, under the assumption that the whistler waves have a fixed amplitude of 100 pT, chorus quasi-linear pitch-angle-diffusion coefficients for 1-MeV electrons near the loss cone have values of $D_{\alpha\alpha}\,{\le}1\times10^{-5}\,radians^2/s\,{=}\,3.3\times$ 10^{-2} degree²/s (Fig. 6g of Orlova et al. (2012)). This D_{qq} value agrees with the chorus-wave electron diffusion coefficients of Horne et al. (2013) for 2 < Kp < 3 at L = 7 in the postmidnight magnetosphere. An L = 7 dipole field line has a distance of about 8.5R_E from the equator to the atmosphere: a 1-MeV electron (v = 2.83×10^{10} cm/s) makes the 8.5-R_E flight in a time of about t = 0.2 s. Using the bounce-averaged pitch-angle diffusion equation $\partial f/\partial t = D_{\alpha\alpha} \partial^2 f/\partial \alpha^2$ the amount of quasi-linear angular scattering $\Delta\alpha$ that would occur during the 0.2-s flight to the atmosphere can be estimated as $\Delta\alpha=(D_{\alpha\alpha}t)^{1/2}=0.08^{\circ},$ a value that is much smaller than the loss-cone size. Even in the dawn sector where whistler chorus is most prevalent, the wave amplitudes are generally below 100 pT (cf. Fig. 6 of Horne et al. (2013)). This calculation estimates that there should not be appreciable scattering of MeV beam electrons by magnetospheric plasma waves.

For electron beams with energies of 10's of keV (energies similar to those of substorm-injected electrons), whistler-mode chorus waves are the strongest scatterers. The lower the energy of the electrons, the stronger the pitch-angle diffusion coefficient and the stronger the

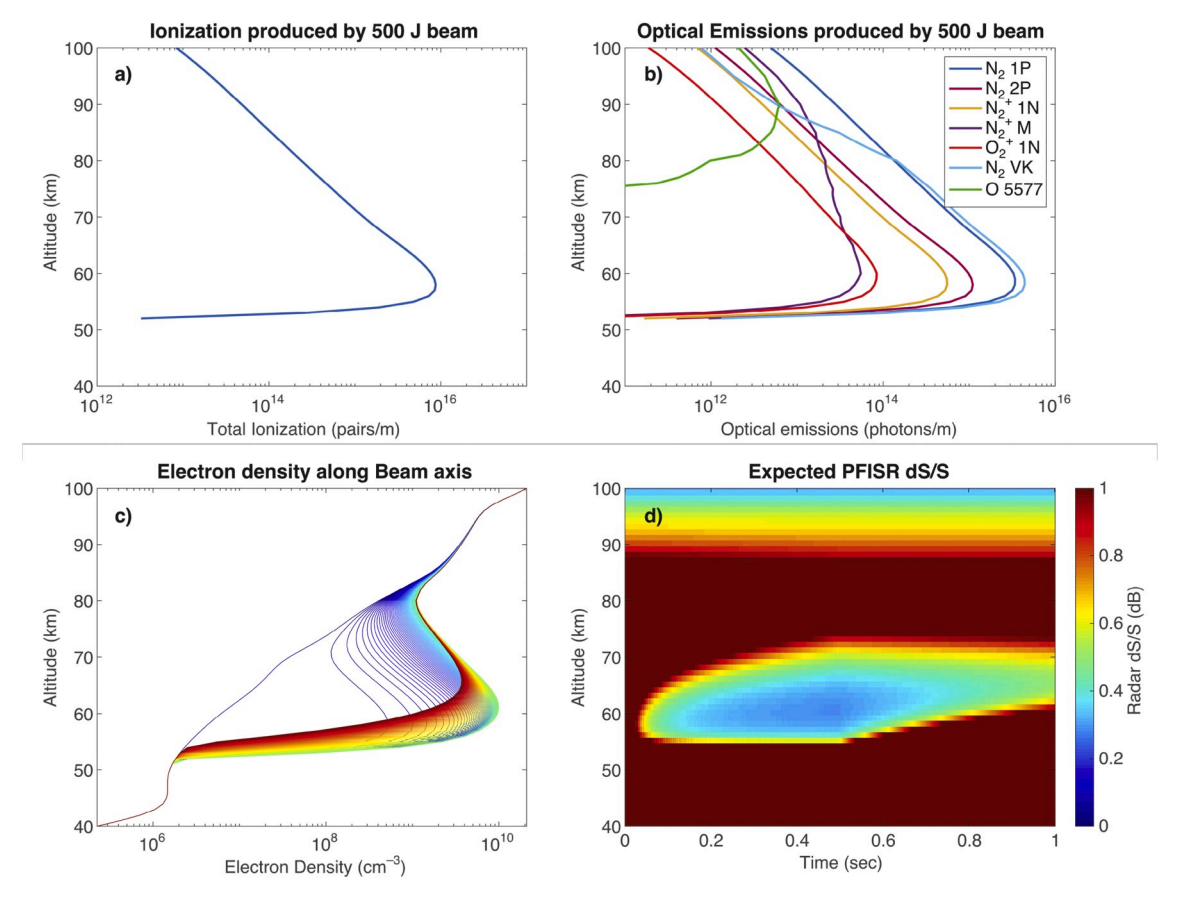


Fig. 6. a) Ionization produced by $500 \, J$ injection of 1 MeV electrons over $0.5 \, s$. b) Optical emissions produced by the same beam. c) Electron density evolution from t = 0 (blue) to $t = 1 \, s$ (red). d) Poker Flat Incoherent Scatter radar predicted dS/S, providing a measure of detectability of the beam. (For interpretation of the references to color in this figure legend, the reader is referred to the Web version of this article.)

angular scattering. In the nightside magnetosphere at 7 R_E under average geomagnetic activity (2 < Kp < 3), the Horne et al. (2013) quasi-linear whistler-mode chorus bounce-averaged pitch-angle diffusion coefficients for 30-keV electrons are $D_{\alpha\alpha}=1.1\times 10^{-5}~radians^2/s=$ $3.6\times 10^{-2}~\text{degree}^2/\text{s}$ in the premidnight region and $D_{\alpha\alpha}=1.1\times 10^{-4}$ $radians^2/s = 3.6 \times 10^{-1} degree^2/s$ in the postmidnight region. (The postmidnight region is the region of diffuse and pulsating aurora, driven by chorus-wave electron scattering.) A 30-keV electron has a speed of 1.0×10^{10} cm/s and makes the 8.5-R_E flight to the atmosphere in t = 0.5 s. The quasi-linear angular scattering by chorus is $\Delta\alpha = (D_{\alpha\alpha}t)^{1/2} = 0.14^{\circ}$ in the premidnight region and the angular scattering is $\Delta \alpha = (D_{\alpha\alpha}t)^{1/2} =$ 0.43° in the postmidnight region. These values are both smaller than the $\sim 2.5^{\circ}$ radius of the loss cone. Additionally, some of that angular scattering occurs away from the equator and, since the local loss cone widens as the electron approaches the Earth, the scattering occurring away from the equator is not effective at moving the electron out of the loss cone.

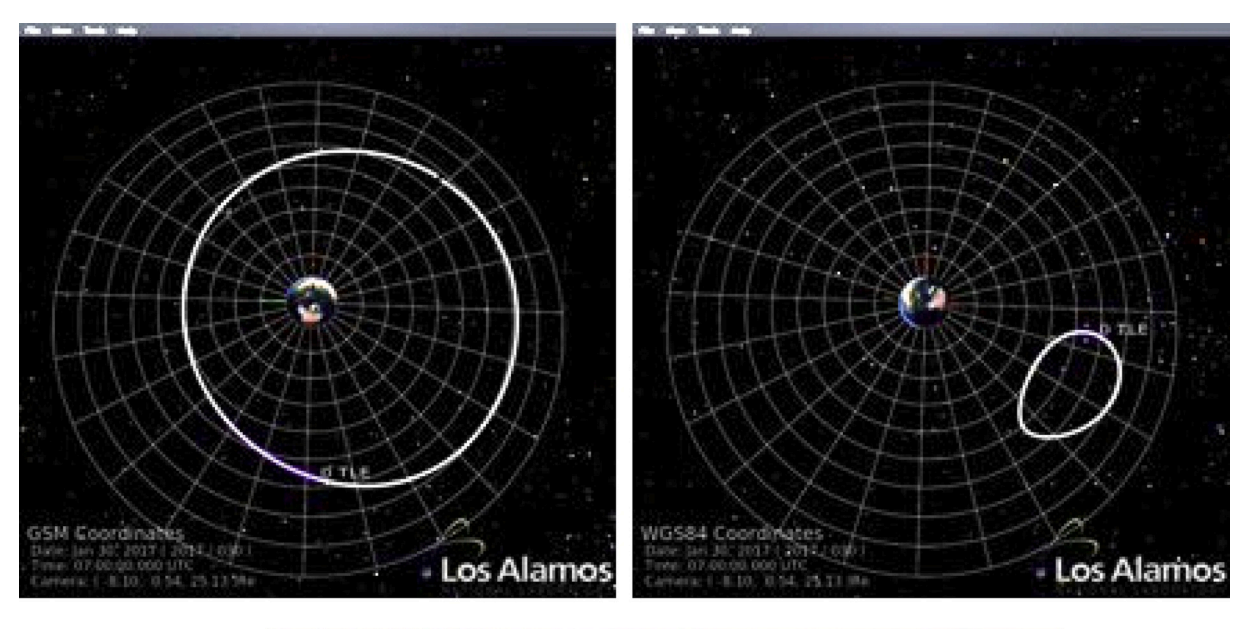
The nonlinear scattering of the beam electrons by large-amplitude and/or coherent whistler-mode waves (e.g. Albert, 2000; Bortnik et al., 2008; Omura et al., 2015; Mourenas et al., 2018) has not yet been assessed.

Another form of scattering comes about at higher energies: the stochastic scattering of the beam electrons by the curvature of magnetic-field lines (Dragt and Finn, 1976; Anderson et al., 1997; Young et al., 2008). Avoiding the use of an MeV beam in the near-Earth magnetotail (where the location of the loss cone is not predictable) will avoid stochastic scattering moving the beam electrons out of the loss cone. Analyses detailing the criteria for the onset of electron-beam stochastic scattering in the magnetotail is reserved for a future publication.

7. Beamspot detection

For magnetic-field-line mapping using an electron beam, detection of the beam footpoint in the upper atmosphere is fundamental. As previous lower-energy experiments have demonstrated (e.g. Davis et al., 1980; Hallinan et al., 1990), the beam can be detected by means of its optical signature. As an example, if the velocity vectors of a 1-MeV beam of electrons are exactly aligned with the Earth's magnetic field at the top of the atmosphere, the 1-MeV electrons will deposit their energy in a narrow altitude range with a peak at about 58 km. If the beam is fired into the loss cone but not at the center of the loss cone, the beam electrons will enter the atmosphere with more-oblique velocity vectors and the energy deposition will be at higher altitudes. Through collisions with atmospheric neutrals, the beam-atmosphere interaction leads to ionization and excitation of N_2 molecules. The 427.8 nm optical band (first-negative band) of the radical N_2^+ will be used for detection of the beam.

Following the theoretical work of Krause (Krause, 1998; Habash Krause et al., 2000), Marshall et al. (2014) investigated the diagnostics for beams with energies ranging from 100 keV to 10 MeV. More recently, Marshall et al. (2019) investigated a 1 MeV beam of electrons, with a duration of 0.1 or 1.0 s, and a total injected energy of 100 J or 1 kJ. Fig. 6 provides a summary of the optical and radar diagnostics for a magnetic-field-aligned beam of 1 MeV electrons, injected over 0.5 s, with an average current of 1 mA, for a total energy of 500 J and an average beam power of 1 kW. The beam spreads in the atmosphere due to collisions, reaching a radius of 300 m at the peak deposition altitude. Fig. 6a shows the total ionization profile, integrated over the beam profile and the duration of the beam, resulting in ionization pairs per meter of altitude. The peak occurs at 58 km altitude, which depends



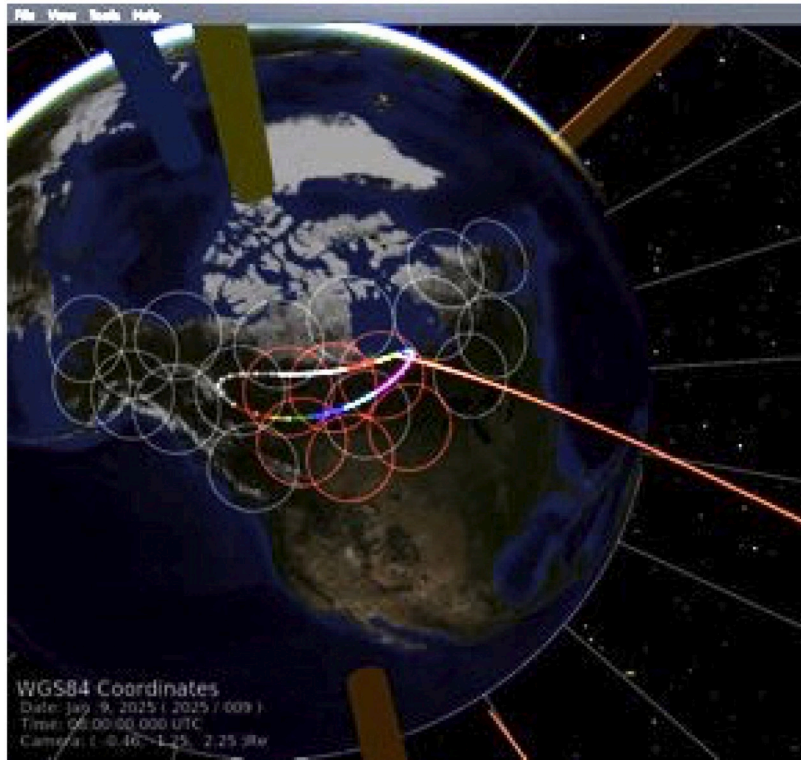


Fig. 7. A 5×8 12° inclination geosynchronous orbit (24-hr period) for possible use in the electron-beam mission. (a. upper left) Orbit in GSM coordinates, (b. upper right) orbit in GEO coordinates, (c. bottom) magnetic footpoint of the orbit over the TREx imaging array in Canada. The magnetic footpoint is shown for Jan 9, 2025 and a magnetic field line is shown at 8UT. The color-coding of the footpoint path shows how close the spacecraft is to the minimum-B point as measured along the field line (red, yellow, green are $<1.0~R_E$, $<0.5~R_E$, $<0.5~R_E$, respectively from the minimum-B point and in the northern hemisphere, while magenta, cyan, blue are $<1.0~R_E$, $<0.5~R_E$ respectively from the minimum-B point and in the southern hemisphere). The red curve is a sample magnetic-field line. (For interpretation of the references to color in this figure legend, the reader is referred to the Web version of this article.)

slightly on the background atmosphere profile used, and has a full-width at half-maximum of 9 km in altitude. Hence, the optical "beam-spot" will be an emitting magnetic-field-aligned column \sim 0.6 km in diameter and \sim 9 km in length at an altitude of about 60 km. From the ionization profile, the optical emissions are calculated, as shown in Fig. 6b. While the N₂ Vegard-Kaplan (VK) and First Positive (1P) band systems are the brightest, these are spread over a wide range of visible and infrared wavelengths, making detection difficult. Instead, we focus on the N₂⁺ first negative band (1N) system (yellow curve), which has prominent

bands peaking at 391.4 nm and 427.8 nm. The 391.4-nm band is brighter than the 427.8-nm band by a factor of 3 (Omholt, 1971), but the shorter-wavelength 391.4-nm light suffers from stronger atmospheric attenuation by Rayleigh scattering. For 427.8 nm, the exponential attenuation coefficient for aerosol-free STP air is 0.037 km $^{-1}$ (Penndorf, 1957; ITT, 1977), which is an e-folding distance of 27 km at 760 Torr. At low atmospheric pressures, a 1-kW electron beam will produce 1.1 W of 427.8 nm emission (Bryant et al., 1970). The critical N₂ neutral number density for collisional quenching of the N₂⁺ first negative band is 3.6 ×

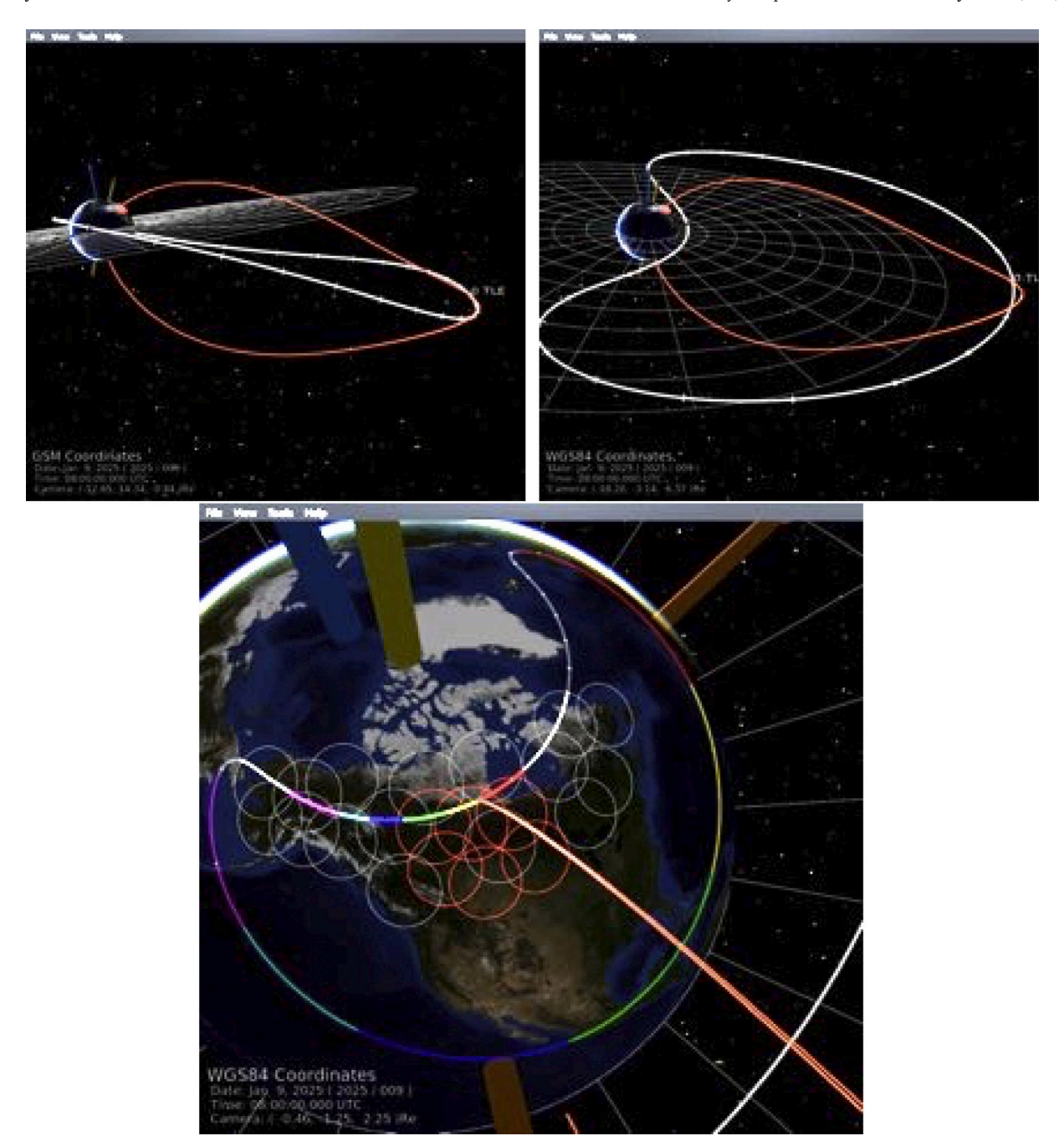


Fig. 8. A 1.3×12 geosynchronous orbit (24-hr period) for possible use in the electron-beam mission. (a. upper left) Orbit in GSM coordinates, (b. upper right) orbit in GEO coordinates, (c. bottom) magnetic footpoint of the orbit over the TREx imaging array in Canada. The magnetic footpoint is shown for Jan 9, 2025 and a magnetic field line is shown at 8UT. The color-coding of the footpoint path shows how close the spacecraft is to the minimum-B point as measured along the field line (red, yellow, green are $<1.0~R_E$, $<0.5~R_E$, $<0.25~R_E$ respectively from the minimum-B point and in the northern hemisphere while magnetic, cyan, blue are $<1.0~R_E$, $<0.5~R_E$ respectively from the minimum-B point and in the southern hemisphere). The red curves are sample magnetic-field lines. (For interpretation of the references to color in this figure legend, the reader is referred to the Web version of this article.)

 $10^{16}~\rm cm^{-3}$ (cf. Table 4.7 of Jones (1974)). At 58 km the N_2 neutral density is about $5\times 10^{15}~\rm cm^{-3}$ (Hedin, 1987), so quenching will reduce the optical power of the beam-spot. Shooting obliquely to the magnetic field to raise the beam-spot altitude could improve spot detection and also bring the beam-spot closer to the aurora, which occur at altitudes above 100 km (Boyd et al., 1971; Sangalli et al., 2011). A 1-kW 10's-of-eV electron beam will produce 1.1 W of 427.8-nm emission, but at the higher beamspot altitude quenching will not reduce the beamspot emission.

The time-dependent ionization profile (pairs/m³/sec) is used in the Glukhov-Pasko-Inan (GPI) chemistry model (Glukhov et al., 1992;

Lehtinen and Inan, 2007) to calculate the perturbation to the D-region electron density for a 1-MeV beam. The result shown in Fig. 6c shows a dramatic increase in the background electron density over the beam area of 300 m radius. Representing the beam from a radio-frequency accelerator, this total energy is divided into pulses of 500 μ s at 10 mA current, spaced every 5 ms, for an average current of 1 mA. The ionization profiles shown in Fig. 6c are following each pulse, separated by 5 ms, and cover a total duration of 1 s, i.e. an extra 0.5 s after the beam duration. This extra 0.5 s is included to show the rapid recovery of the electron density perturbation, due to high electron-attachment rates at these low altitudes. From the electron density perturbation, a radar

signature can be calculated, following the method outlined in Marshall et al. (2019). Fig. 6d shows the resulting radar dS/S, the relative noise power in the radar signal. Values below dS/S = 1 are theoretically detectable by the incoherent scatter radar such as the one in Poker Flat, Alaska, not accounting for technical issues such as radar integration times. At higher altitudes, the beamspot of a 10's of keV beam will have an ionization perturbation that persists longer, making radar detection easier.

The optical signatures observed from the ground scale linearly with the total energy deposited in the atmosphere; hence the 1 kJ beam results in ten times higher optical emissions compared to the 100 J beam. On the other hand, the electron density perturbation (Fig. 6c) is nonlinear with the electron and beam energy. Higher electron energies deposit lower in altitude, where electron attachment is faster; hence the impact at lower altitudes is diminished. Similarly, a higher total beam energy will increase the electron density perturbation, but with a less-than-linear response, again because the higher ionization rate leads to more recombination. This effect can be seen in Fig. 6c, where successive pulses increase the electron density, but each with a lesser impact than the previous, especially at lower altitudes.

The X-ray signature from a 1-MeV electron beam is likely too weak to be reliably detected. Furthermore, it requires either balloon- or spacecraft-based detectors, making the fortuitous conjunction between the beam-spot and the detector unlikely.

It is straightforward to estimate the optical signal on the ground from the optical emissions in Fig. 6b. We take the optical emission rates in each altitude bin (photons per km of altitude per second, during the 1kW 0.5-s beam deposition period), and propagate them through an atmosphere to the ground using a radiative transfer code such as MOD-TRAN. These result in a photon flux at the ground, in photons per unit area per second. The calculation is repeated for each optical emission presented in Fig. 6b. We then integrate in wavelength across the product of the instrument wavelength response and the emission band spectrum to estimate the in-band photon flux. Using the photon emission profiles in Fig. 6b for N₂⁺ 1N (yellow curve), assuming an instrument with a 10 nm passband around the 427.8 nm bandhead, and assuming that the beam spot is directly over the camera, we calculate an expected flux of 8.0×10^6 photons/m² at the ground, integrated over the 0.5 s beam period. If the cameras used for the beam-spot detection have effective apertures (factoring in camera efficiency) of 10 cm², so the overhead beam-spot will put 6000 photons into the camera. This is sufficient for the beam-spot to be seen against a fairly bright auroral background. For instance, if the auroral background is 1 kR in intensity in the 427.8-nm band, then each square cm of the sky would emit 10^9 photons/s into 4π steradian. If a pixel in the sky at 100-km altitude has an area of 1 km², that pixel would emit 10^{19} photons/s of 427.8 nm. At the ground a distance d = 100 km away, the flux of auroral 427.8 nm photons from that sky pixel would be $10^{19}/(4\pi d^2) = 8 \times 10^3$ photons/cm²/sec. With a 10-cm^2 effective camera aperture, this is 4×10^4 auroral photons into the camera in 0.5 s. The statistical noise of the 4×10^4 auroral photons is $(4 \times 10^4)^{1/2} = 200$ photons. Even with the 6000 beamspot photons spread over several pixels, the beamspot signal is well above the 200 photons per pixel noise of the auroral background. Using a beam on-off blinking sequence coordinated with the camera also makes the beam easier to detect in the presence of auroral emissions.

If the beamspot is not directly above the camera then the beamspot detection is more difficult owing to the $1/d^2$ geometric falloff of the photon flux (where d is the distance between the spot and the camera) and the exponential atmospheric attenuation of the photon flux owing to Rayleigh scattering.

Ideal for this magnetospheric beam experiment, an array of optical all-sky cameras across Canada (an extension of the TREx 6-camera array (Spanswick et al., 2018)) is beginning its operation. Each TREx camera has an approximately 2000 km \times 1000 km field of view of the upper atmosphere. The cameras are multispectral imagers collecting 427.8 nm, 557.7 nm, near-infrared, and full-color optical images with high time

cadence for the 427.8 nm images. Within the field of the TREx camera array there are also meridian imaging spectrographs, imaging riometers, and total-electron-content detectors. The high-time-cadence 427.8 nm images will be processed in coordination with the accelerator on-off blink sequence to maximize the beam-spot detection in the presence of auroral 427.8 nm emission.

8. Orbit choices

Numerous orbits have been analyzed for an auroral-electron-beam mission. Focusing on the ground-based camera network situated in Canada (Spanswick et al., 2018), most of the orbits considered feature periodic revisits of the magnetic footprints over the TREx observing array. One of the most-promising orbits is the so-called "inclined geosynchronous" orbit. This orbit is a "5 \times 8" elliptical 24-hour (sidereal) orbit with 12° inclination. (5 \times 8 means perigee is at $5R_E$ and apogee is at $8R_E$.) Note that in order to obtain a 24-hr period, the major axis (apogee plus perigee) must be $\sim \! 13.2R_E$ in total length. Fig. 7 shows this orbit in GSM coordinates (Fig. 7a) as well as geographic (GEO) coordinates (Fig. 7b). Note that in GEO coordinates, the orbit executes a closed loop with apogee over Canada. A typical trajectory of the magnetic footpoint of this orbit over Canada is shown in Fig. 7c.

The main advantages of the 5×8 inclined geosynchronous orbit are that: (1) the spacecraft samples a range of field lines in the magnetospheric dipole-to-magnetotail transition region very well; (2) apogee is always over Canada; (3) the magnetic footpoint wanders over a small set of ground-based all-sky imagers, (4) the 5-R_E perigee allows the spacecraft to avoid the harsh radiation belts almost all of the time which reduces shielding requirements. The main disadvantages of this orbit are two-fold: (1) The apogee being at 8R_E means we may not always be near the minimum-magnetic-field-strength (~equatorial) point on the field lines which may reduce mapping capabilities at times, and (2) a 5 \times 8 orbit is costly because (a) an extra boost motor must be carried into orbit to raise perigee and (b) end-of-life plans would require considerable fuel to either lower perigee for de-orbiting or raising perigee to place the magnetospheric spacecraft into a super-synchronous "graveyard" orbit. The furthest out that this orbit can sample the minimum-B region is 8 R_E, but since the orbit is inclined, since the orbit precesses, and since the location of the minimum-B surface varies with dipole tilt and with geomagnetic activity, the spacecraft would not always cross the minimum-B surface at the same distance from the Earth. Note that the auroral-arc generator mechanisms operate over a large portion of the auroral-arc flux tube (cf. Fig. 1), not just at the equator (minimum-B region), so the generator mechanism can be discerned by the magnetospheric spacecraft wherever the spacecraft crosses the auroral-arc field lines.

Another orbit that has very attractive properties is a 24-hr highly elliptical " 1.3×12 " orbit. This also maintains apogee over Canada, but has a much less confined magnetic footpoint path over Canada. Fig. 8 shows this orbit in GSM and GEO coordinates as well as the large ground magnetic footpoint over Canada. The main advantages of the 1.3×12 RE 24-hr orbit are: (1) apogee is maintained over Canada for long periods of time, (2) the lower perigee eliminates the need for costly boost motors and (3) the lower perigee greatly simplifies end-of-life deorbiting operations, (4) the spacecraft spends more time in the more stretched portions of the dipole-to-magnetotail transition region. The main disadvantages are: (1) the loss cone is smaller at these larger distances and the magnetic field strength is lower which necessitates greater pointing accuracy for beam-firing, (2) if a relativistic beam is used estimation of the location of the loss cone is difficult, and (3) the ground magnetic footpoint is not well-contained over a small number of ground-based imagers which may necessitate placement of additional imagers along the footpoint path. The furthest out that this orbit can sample the minimum-B region is 12 R_E, and the discussion at the end of the previous paragraph is also appropriate here: the generator mechanism can be discerned by the magnetospheric spacecraft when the

spacecraft crosses the auroral-arc field lines away from the minimum-B surface.

9. Magnetospheric measurements needed

To determine the magnetospheric driver mechanisms of auroral arcs, spatial gradients in the magnetosphere must be measured as the illuminated spacecraft footpoint crosses the optical auroral arcs. In particular the following gradients must be measured: the ion plasma pressure, the electron plasma pressure, the ion and electron temperature anisotropy, the plasma mass density, the magnetic-field strength, and the plasma flow vector, with the gradients in the plasma flow vector $\underline{\mathbf{v}}$ taking the forms $\nabla \times \underline{\mathbf{v}}$ (flow shear) and $(\underline{\mathbf{v}} \bullet \nabla)\underline{\mathbf{v}}$ (flow braking). Gradients in the magnetic-field strength represent gradients in the flux-tube volume.

Gradients in the magnetosphere can be measured (1) instantaneously using an array of daughter spacecraft near the main electron-beam spacecraft or (2) using the single electron-beam spacecraft as its optical footpoint crosses the auroral forms. (It is more-accurately stated that gradients are measured as auroral forms pass over the spacecraft.) The single spacecraft crossing the arc measures predominantly the cross-arc gradient which has a much shorter gradient scale than along-the-arc gradients: multiple spacecraft can measure both the steeper cross-arc gradient and the shallower along-the-arc gradient (cf. the cross products on the right-hand side of expression (1)). Multiple daughter spacecraft are desirable, but costly. Cross-arc (radial) gradient scales in the magnetosphere are expected to be a few-hundred km near geosynchronous orbit and 1000-km or so further out (cf. Section 2.1), so spacecraft separations of these scales are optimal.

It is important to measure electron flow \underline{v}_e and ion flow \underline{v}_i separately. In thin-current-sheet models of the auroral-arc driving (Birn et al., 2004a,b, 2012; Sergeev et al., 2012 Hseih and Otto, 2014), perpendicular electric fields form around the current sheets; with magnetospheric ions and electrons having different-sized gyroradii, the ions and electrons flow differently near the thin current sheets, producing new Hall currents. The occurrence of $\underline{v}_i \neq \underline{v}_e$ is a signature of this auroral driving mechanism. The electron flow \underline{v}_e can be measured with an electron drift instrument (e.g. Paschmann et al., 1998; Torbert et al., 2016) (which also yields measurements of the electric field) and the ion flow \underline{v}_i can be measured with a plasma particle instrument (e.g. Bame et al., 1993).

In order to measure quantities critical to identifying the mechanisms of auroral-arc driving, the minimum magnetospheric instrumentation should include (1) a magnetometer capable of measuring the magnetic-field strength and direction, (2) an ion detector (1 eV - 40 keV) capable of measuring the hot-proton number density, proton temperature, proton temperature anisotropy, and proton pressure, (3) an electron detector (1 eV - 40 keV) capable of measuring the hot-electron number density, electron temperature, electron temperature anisotropy, and electron pressure, and (4) an electron flow instrument. Note that in the near-Earth portion of the plasma sheet the hot-electron and hot-ion number densities need not be equal (Thomsen et al., 1998), with hidden populations of cool electrons ensuring charge neutrality.

Using the values of the standard low-latitude growth-phase arc in Table 1, estimates of the measurement requirements and measurement accuracies near the magnetospheric equator are calculated and entered into Table 3. Most of the values in Table 3 are easily attained. One value that is critical and somewhat difficult to obtain is the 0.5° accuracy needed for the magnetic-field direction. This accuracy is critical for pointing the electron beam into the atmospheric loss cone. Fortunately, an electron drift instrument, which works in concert with a magnetometer, provides offset corrections to the magnetometer about the direction of the magnetic field (Torbert et al., 2014). A second accuracy that is difficult to obtain is the 1.5 km/s requirement for the plasma flow velocity across the arc. This measurement is useful for obtaining a complete picture of how auroral arcs are driven and for quantifying power-conversion calculations.

Beyond the four minimum required instruments listed above, other

Table 3Measurement requirements in the magnetosphere.

Measurement Quantity	Symbol	Typical Value	Desired Accuracy	Method of Determining Desired Accuracy
proton number density	n_p	$1~\mathrm{cm}^{-3}$	$0.1~{\rm cm}^{-3}$	10% of ambient value
proton temperature	T_p	10 keV	1 keV	10% of ambient value
proton pressure	P_{p}	1.6 nPa	0.16 nPa	10% of ambient value
proton pressure	P _{p⊥} -	0.16		10% of ambient
anisotropy	$P_{p }$	nPa		pressure
electron number density	n _e	1 cm ⁻³	$0.1~{\rm cm}^{-3}$	10% of ambient value
electron temperature	T _e	2 keV	200 eV	10% of ambient value
electron pressure	P_{e}	0.32 nPa	0.03 nPa	10% of ambient value
electron pressure anisotropy	$P_{e\perp}$ - $P_{e }$	0.03 nPa		10% of ambient pressure
proton flow along arc	V _p -	150 km/s	15 km/s	10% of expected value
electron flow along arc	Ve-	150 km/s	15 km/s	10% of expected value
proton or electron flow across arc	<u>V</u> radial	6.6 km/ s	1.5 km/s	25% of expected value
magnetic-field direction vector	<u>b</u>		0.5°	Required loss-come aiming
magnetic-field strength	B_{mag}	80 nT	1 nT	Commensurate with loss-cone aiming

instruments that would help to understand the magnetospheric driving of auroral arcs are the following. (5) Energetic particle measurements (40 keV-500 keV) would help to understand the environment in which auroral arcs are driven. This will be particularly valuable for understanding the driving of active arcs during substorms. In the near-Earth plasma sheet proton measurements above 40 keV are required to get the total ion pressure (Borovsky et al., 1998b), particularly during geomagnetically active times. (6) A measurement of the cold-plasma number density would also help to understand the environment in which auroral arcs are driven, and the proximity of the growth-phase arcs to the plasmapause. Cold-plasma measurements would also determine if there is any systematic role that cold ions or cold electrons play in the driving and location of auroral arcs. Cold-electron number density is straightforward to obtain with a wave-electric-field instrument (Benson et al., 2004). (7) An instrument that can measure field-aligned (upflowing) electrons and ions would be of use to understand the arc-ionosphere system: the role of arcs in ion outflows and the role of arc return currents in electron outflows.

The scientific focus of this mission concept is the cause of auroral arcs. However, the four minimum-required magnetospheric instruments are more-or-less sufficient for investigating the causes of other discrete auroral forms (e.g. auroral streamers, omega bands, black arcs, giant undulations, etc.). The cause of diffuse aurora, although not fully understood, is less of an outstanding issue. It is generally believed that diffuse aurora is caused by the pitch-angle scattering of magnetospheric electrons and ions into the atmospheric loss cone by magnetospheric plasma waves (Chen and Schulz, 2000; Yahnin and Yahnina, 2007; Thorne et al., 2010; Ni et al., 2016) or the scattering of protons into the loss cone by stretched magnetic-field geometries (e.g. Sergeev et al., 1983). If the focus of the mission increased to include the cause of diffuse aurora, then a plasma-wave instrument would need to be added to the magnetospheric spacecraft, and measurements of the cold-plasma density would also be essential. A plasma (electric) wave instrument would also provide measurements of the total electron density, accounting for plasma too cold for the plasma instrument to detect.

10. Summary

A mission has been outlined to provide unambiguous measurements

that will bring closure to the important question: How does the magnetosphere generate auroral arcs? Answering this question will allow us to discern the impact that the aurora has on the evolution and dynamics of the magnetosphere and will allow us to look at the aurora and discern what it tells us about processes ongoing in the magnetosphere.

Decades of research went into the design of this mission. The core of the experiment is an electron-beam source designed for spaceflight into the magnetosphere. Coordinating the pulsing of the electron beam with observations by a network of ground-based optical cameras imaging the upper atmosphere that detect the aurora and the pulsed electron beam. Several technical issues have been overcome, including an understanding of how to mitigate spacecraft charging of the accelerator platform, how to aim and propagate the electron beam, and how to detect the beam from the ground.

Several tradeoffs are available in the design of this mission. Selecting the optimal beam energy involves a trade of the ability to aim the beam into the actual atmospheric loss cone versus the severity of spacecraft charging. The selection of the optimal orbit involves considerations of camera coverage versus regions of the magnetosphere visited. The selection of the scientific instruments carried with the accelerator involves consideration of the existing theories of auroral-arc generation by the magnetosphere. In measuring gradients in the magnetosphere there is a tradeoff between a single spacecraft versus a mother spacecraft with daughters.

This electron-beam experiment can also solve other important science issues dealing with the causes of other types of aurora, the impacts of all types of aurora on the magnetosphere, magnetosphere-ionosphere coupling, atmospheric chemistry, atmospheric electricity, and magnetic-field-line mapping (cf. Appendix).

This electron-beam experiment is geared to the science of the magnetospheric, ionospheric, and auroral communities with opportunities to mount campaigns utilizing ground-based and balloon-borne instrumentation and other satellite-based magnetic conjunctions.

Acknowledgements

The authors thank Matt Argall, Joachim Birn, Mick Denton, Eric Donovan, John Dorelli, Phil Fernandes, Gerhard Haerendel, Larry Kepko, Dave Knudsen, Oleksandr Koshkarov, Brian Larsen, Omar Leon, John Lewellen, Liz McDonald, Jeff Neilson, Antonius Otto, Noora Partamies, John Raitt, Geoff Reeves, Vadim Roytershteyn, Jan Sojka, Emma Spanswick, Maria Usanova, Hans Vaith, Jesse Walsh, and Kateryna Yakymenko. Work at the Space Science Institute was supported by NASA Heliophysics LWS TRT program via grant NNX14AN90G, by the NSF GEM Program via award AGS-1502947, by the NASA Heliophysics Guest Investigator Program via grant NNX17AB71G, and by the NSF SHINE program via award AGS-1723416.

Appendix. Other Science

With the magnetospheric electron beam experiment, a number of scientific problems beyond the auroral-arc generator can be investigated.

- (1) Determine the Causes of Other Types of Aurora. The magnetospheric causes of other common types of aurora are also unknown and this electron-beam experiment can shed light on the magnetospheric mechanisms acting to produce them. These include breakup arcs, black arcs, omega bands, giant undulations, and torches.
- (2) Connecting Magnetospheric Phenomena with Ionospheric Phenomena. With the electron-beam mapping procedure there are several magnetospheric phenomena and boundaries for which the ionospheric counterpart could be identified: the plasmapause, the inner edge of the electron plasma sheet, the remnant layer, the

- dipole-to-magnetotail transition, substorm injection fronts, flow bursts, etc. Conversely, there are several ionospheric phenomena for which the magnetospheric source can be identified: sub-auroral polarizations streams, ionospheric currents, convection reversals, the Harang discontinuity, the mid-latitude trough, Fregion ionization patches, etc.
- (3) Magnetosphere-Ionosphere Flow Coupling. Combining the electron beam experiment with the global SuperDARN radar array (Bristow et al., 2016), the location of the beam optical spot can be put into the context of SuperDARN ionospheric convection maps to determine when ionospheric flow commences at the location of the optical beam-spot relative to when magnetosphere flow commences at the electron-beam spacecraft. This provides repeated data for the magnetosphere-ionosphere-coupling question of who-drives-whom, when, and where?
- (4) Generation of Plasma Waves. Electron beams on sounding rockets, the space shuttle, and satellites in polar orbit have been used to generate plasma waves and test beam-plasma-interaction theories (Beghin et al., 1984; Neubert et al., 1986; Reeves et al., 1990; Kiraga et al., 1995; Raitt et al., 1995; Huang et al., 1998). Efficient ways to inject plasma waves into the magnetosphere are important for radiation belt remediation (Inan et al., 2003); beams could have advantages over antennas, since the wavelengths of interest can be large (~km for whistler waves) (Carlsten et al., 2018; Delzanno and Roytershteyn, 2019). Using a variable-energy electron beam to generate waves that can be received by other spacecraft would test wave-generation and wave-propagation models and allow us to probe the magnetospheric environment.
- (5) Atmospheric Chemistry. There is scientific interest in the production of NO_x , HO_x , and ozone by the precipitation of relativistic radiation-belt electrons into the middle atmosphere (Verronen et al., 2013; Andersson et al., 2014). The controlled experimentation of these processes with a relativistic electron beam from above combined with ground-based spectroscopy has been suggested (e.g. Neubert et al., 1990; Marshall et al., 2019). The altitude of the beamspot is adjustable by aiming away from the center of the loss cone.
- (6) Ionization-Recombination-Attachment Physics. At lower densities relevant to the middle and upper atmosphere, the physics of free electrons in air is studied in the laboratory (e.g. Wagner, 1971; Schneider and Brau, 1982). Using a relativistic electron beam fired down into the atmosphere has been suggested as a method to study in situ the upper-atmospheric rates of ionization, recombination of ionization, and electron attachment to produce negative radicals and negative ions (Banks et al., 1990; Neubert et al., 1996; Neubert and Gilchrist, 2004).
- (7) Atmospheric Electricity. The creation of a highly conducting (free electron) channel in the Earth's atmospheric electric field by an MeV electron beam, followed in time by a weaker conduction (negative radical) channel after electron attachment occurs, could provide information about the conductivity physics of the upper atmosphere.
- (8) Microburst Electrodynamics. When relativistic-electron microbursts occur, they produce conductivity channels connecting the ionosphere to the middle atmosphere (Rodger et al., 2002, 2004, 2007), delivering positive charge from the ionosphere into the middle atmosphere and then stranding the positive charge as the conductivity channel decays (Borovsky, 2017). These charge-stranding processes and their perturbation of the atmospheric electric field can be simulated in a controlled fashion using an MeV electron beam, with the desired electron beam capable of depositing much more energy than a typical microburst (Lorentzen et al., 2001; Borovsky, 2017).
- (9) Triggering Upward Thundercloud Discharges. The triggering of upward electrical discharges from thunderclouds with the use of a

- relativistic electron beam fired down into the atmosphere has been suggested several times (e.g. Banks et al., 1990; Neubert et al., 1990; Neubert and Gilchrist, 2004; Marshall et al., 2019). An MeV electron beam could provide important tests of the understanding of upward discharges, particularly on mid-latitude magnetic field lines where beam-spot locating would not be
- (10) Improving Magnetospheric Magnetic-Field Models. Every time a beam-spot is located in the upper atmosphere, scientific data is obtained that can be used to improve magnetic-field models of the Earth's magnetosphere. Time-of-flight and loss-cone-shift information can also be used to constrain field-line lengths and field-line curvatures (Willard et al., 2019b).

References

- Aikio, A.T., Lakkala, T., Kozlovsky, A., Williams, P.J.S., 2002. Electric fields and currents of stable drifting auroral arcs in the evening sector. J. Geophys. Res. 107, 1424.
- Akasofu, S.-I., 1963. The dynamical morphology of the aurora polaris. J. Geophys. Res. 68 1667
- Akasofu, S.I., 1965. The aurora. Scientfic Amer 213 (6), 55.
- Albert, J.M., 2000. Gyroresonant interactions of radiation belt particles with a monochromatic electromagnetic wave. J. Geophys. Res. 105, 21191.
- Anderson, B.J., Erlandson, R.E., Zanetti, L.J., 1992, A statistical study of Pc 1-2 magnetic pulsations in the equatorial magnetosphere 1. Equatorial occurrence distribution. J. Geophys. Res. 97, 3075.
- Anderson, B.J., Decker, R.B., Paschalidis, N.P., Sarris, T., 1997. Onset of nonadiabatic particle motion in the near-Earth magnetotail. J. Geophys. Res. 102, 17553.
- Andersson, M.E., Verronen, P.T., Rodger, C.J., Clilverd, M.A., Seppala, A., 2014. Missing driver in the Sun-Earth connection from energetic electron precipitation impacts mesospheric ozone. Nat. Commun. 5, 5197.
- Arnoldy, R.L., 1977. The relationship between field-aligned current, carried by suprathermal electrons, and the auroral arc. Geophys. Res. Lett. 4, 407.
- Atkinson, G., 1978. Review of auroral currents and auroral arcs. J. Geomagn. Geoelectr. 30, 435.
- Bame, S.J., McComas, D.J., Thomsen, M.F., Barraclough, B.L., Elphic, R.C., Glore, J.P., Gosling, J.T., Chavez, J.C., Evans, E.P., Wymer, F.J., 1993. Magnetospheric plasma analyzer for spacecraft with constrained resources. Rev. Sci. Instrum. 64, 1026.
- Banks, P.M., Fraser-Smith, A.C., Gilchrist, B.E., 1990. Ionospheric modification using relativistic electron beams, 485. Specialised Printing Services Limited, Loughton, United Kingdom, 22-1 - 22-18 AGARD (Advis. Group Aerosp. Res. Dev) Conf. Proc.
- Beghin, C., Lebreton, J.P., Maehlum, B.N., Troim, J., Ingsoy, P., Michau, J.L., 1984. Phenomena induced by charged particle beams. Science 225 (4658), 188.
- Benson, R.F., Webb, P.A., Green, J.L., Garcia, L., Reinisch, B.W., 2004. Magnetospheric electron densities inferred from upper-hybrid band emissions. Geophys. Res. Lett. 31, L20803.
- Birn, J., Hesse, M., Haerendel, G., Baumjohann, W., Shiokawa, K., 1999. Flow braking and the substorm current wedge. J. Geophys. Res. 104, 19895.
- Birn, J., Schindler, K., Hesse, M., 2004a. Thin electron current sheets and their relation to auroral potentials. J. Geophys. Res. 109, A02217.
- Birn, J., Schindler, K., Hesse, M., 2004b. Magnetotail aurora connections: the role of thin
- current sheets. Geophys. Monogr. 197, 337. Birn, J., Nakamura, R., Panov, E., Hesse, M., 2011. Bursty bulk flows and dipolarization
- in MHD simulations of magnetotail reconnection. J. Geophys. Res. 116, A01210. Birn, J., Schindler, K., Hesse, M., 2012. Magnetotail aurora connection: the role of thin current sheets. Geophys. MS 197, 337.
- Borovsky, J.E., 1993. Auroral arc thicknesses as predicted by various theories. J. Geophys. Res. 98, 6101.
- Borovsky, J.E., 2002. The magnetosphere-ionosphere observatory (MIO). Los Alamos National Laboratory. https://www.lanl.gov/csse/MIOwriteup.pdf.
- Borovsky, J.E., 2017. Electrical conductivity channels in the atmosphere produced by relativistic-electron microbursts from the magnetosphere. J. Atmos. Sol. Terr. Phys. 155, 22,
- Borovsky, J.E., Bonnell, J., 2001. The dc electric coupling of flow vortices and flow channels in the magnetosphere to the resistive ionosphere. J. Geophys. Res. 106,
- Borovsky, J.E., Delzanno, J.L., 2019. Space active experiments: the future. Front. Astron. Space Sci. 6, 31.
- Borovsky, J.E., Denton, M.H., 2010. The magnetic field at geosynchronous orbit during high-speed-stream-driven storms: Connections to the solar wind, the plasma sheet, and the outer electron radiation belt. J. Geophys. Res. 115, A08217.
- Borovsky, J.E., Greenwald, R.A., Hallinan, T.J., Horwitz, J.L., Kelley, M.C., Klumpar, D. M., Lysak, R.L., Mauk, B.H., Moore, T.M., Reeves, G.D., Singer, H.J., Thomsen, M.F., 1998a. The Magnetosphere-Ionosphere Facility: a satellite cluster in geosynchronous orbit connected to ground-based observatories. Eos Trans. Amer. Geophys Union 79 (45), F744.
- Borovsky, J.E., Suszcynsky, D.M., Buchwald, M.I., DeHaven, H.V., 1991. Measuring the thicknesses of auroral curtains. Arctic 44, 231.

- Borovsky, J.E., Thomsen, M.F., Elphic, R.C., Cayton, T.E., McComas, D.J., 1998b. The transport of plasma-sheet material from the distant tail to geosynchronous orbit. J. Geophys. Res. 103, 20297.
- Borovsky, J.E., Delzanno, G.L., Valdivia, J.A., Moya, P.S., Stepanova, M., Birn, J., Blum, L.W., Lotko, W., Hesse, M., 2020a. Outstanding questions in magnetospheric plasma physics: the Pollonzo view. J. Atmos. Sol. Terr. Phys. submitted to JASTP-D-20-00153
- Borovsky, J.E., Birn, J., Echim, M.M., Fujita, S., Lysak, R.L., Knudsen, D.J., Marghitu, O., Otto, A., Watanabe, T.-H., Tanaka, T., 2020b. Quiescent discrete auroral arcs: a review of magnetospheric generator mechanisms. Space Sci. Rev. 216, 1.
- Bortnik, J., Thorne, R.M., Inan, U.S., 2008. Nonlinear interaction of energetic electrons with large amplitude chorus. Geophys. Res. Lett. 35, L21102.
- Boyd, J.S., Belon, A.E., Romick, G.J., 1971. Latitude and time variation in precipitated electron energy inferred from measurements of auroral height. J. Geophys. Res. 76,
- Bristow, W.A., Hampton, D.L., Otto, A., 2016. High-spatial-resolution velocity measurements derived using Local Divergence-Free Fitting of SuperDARN observations. J. Geophys. Res. 121, 1349.
- Bruning, K., Goertz, C.K., 1986. Dynamics of a discrete auroral arc. J. Geophys. Res. 91,
- Bryant, D.A., Courtier, G.M., Skovli, G., Linalen, H.R., Aarsnes, K., Maseide, K., 1970. Electron density and electron flux in a glow aurora. J. Atmos. Terr. Phys. 32, 1695.
- Burke, W.J., Machuzak, J.S., Maynard, N.C., Basinski, E.M., Erickson, G.M., Hoffman, R. A., Slavin, J.A., Hanson, W.B., 1994. Auroral ionospheric signatures of the plasma sheet boundary layer in the evening sector. J. Geophys. Res. 99, 2489.
- Carlsten, B.E., Colestock, P.L., Cunningham, G.S., Delzanno, G.L., Dors, E.E., Holloway, M.A., Jeffrey, C.A., Lewellen, J.W., Marksteiner, Q.R., Nguyen, D.C., Reeves, G.D., Shipman, K.A., 2018. Radiation-belt remediation using space-based antennas and electron beams. IEEE Trans. Plasma Sci. 47, 2045.
- Chen, M.W., Schulz, M., 2000. Simulations of diffuse aurora with plasma sheet electrons in pitch angle diffusion less than everywhere strong. J. Geophys. Res. 106, 28949. Child, C.D., 1911. Discharge from hot Ca). Phys. Rev. 32, 492.
- Clausen, L.B.N., Baker, J.B.H., Ruohoniemi, J.M., Singer, H.J., 2011. EMIC waves observed at geosynchronous orbit during solar minimum: statistics and excitation. J. Geophys. Res. 116, A10205.
- Colandrea, C., 2018. Model to study the expansion of plasma contactor emitted by a magnetospheric spacecraft to mitigate charging effects. Master's Degree Thesis. Politecnico di Torino, Italy. https://webthesis.biblio.polito.it/7838/1/tesi.pdf.
- Colpitts, C.A., Hakimi, S., Cattell, C.A., Bombeck, J., Maas, M., 2013. Simultaneous ground and satellite observations of discrete auroral arcs, substorm aurora, and Alfvenic aurora with FAST and THEMIS GBO. J. Geophys. Res. 118, 6998.
- Comfort, R.H., Moore, T.E., Craven, P.D., Pollock, C.J., Mozer, F.S., Williamson, W.S., 1998. Spacecraft potential control by the plasma source instrument on the POLAR satellite, J. Spacecraft Rockets 35, 845.
- Coroniti, F.V., Pritchett, P.L., 2014. The quiet evening auroral arc and the structure of the growth phase near-Earth plasma sheet. J. Geophys. Res. 119, 1827.
- Dahlgren, H., Ivchenko, N., Sullivan, J., Lanchester, B.S., Marklund, G., Whiter, D., 2008. Morphology and dynamics of aurora at fine scale: first results from the ASK instrument. Ann. Geophys. 26, 1041.
- Dahlgren, H., Lanchester, B.S., Ivchenko, N., Whiter, D., 2017. Variations in energy, flux, and brightness of pulsating aurora measured at high time resolution. Ann. Geophys. 35, 493,
- Davidson, G., O'Neil, R., 1964. Radiation from nitrogen and air at high pressure excited by energetic electrons. J. Chem. Phys. 41, 3946.
- Davis, T.N., Hess, W.N., Trichel, M.C., Wescott, E.M., Hallinan, T.J., Stenbaek-Nielsen, H. C., Maier, E.J.R., 1980. Artificial aurora conjugate to a rocket-borne electron accelerator. J. Geophys. Res. 85, 1722.
- De Keyser, J., Echim, M., 2013. Electric potential differences across auroral generator interfaces. Ann. Geophys. 31, 251.
- Delzanno, G.L., Roytershteyn, V., 2019. High-frequency plasma waves and pitch angle scattering induced by pulsed electron beams. J. Geophys. Res. 124, 7543.
- Delzanno, G.L., Borovsky, J.E., Thomsen, M.F., Moulton, J.D., 2015a. Beam experiments in the magnetosphere with plasma contactors: the electron collection and ion emission routes. J. Geophys. Res. 120, 3588.
- Delzanno, G.L., Borovsky, J.E., Thomsen, M.F., Moulton, J.D., MacDonald, E.A., 2015b. Beam experiments in the magnetosphere: how do we get the charge off the spacecraft? J. Geophys. Res. 120, 3647.
- Delzanno, G.L., Borovsky, J.E., Thomsen, M.F., Gilchrist, B.E., Sanchez, E., 2016. Can an electron gun solve the outstanding problem of magnetosphere-ionosphere connectivity? J. Geophys. Res. 121, 6769.
- Denton, M.H., 2019. Some unsolved problems of magnetospheric physics. Magnetospheres in the Solar System. AGU Books, Washington DC (in press).
- Denton, M.H., Thomsen, M.F., Korth, H., Lynch, S., Zhang, J.C., Liemohn, M.W., 2005. Bulk plasma properties at geosynchronous orbit. J. Geophys. Res. 110, A07223.
- Denton, M.H., Borovsky, J.E., Stepanova, M., Valdivia, J.A., 2016. Unsolved problems of magnetospheric physics. J. Geophys. Res. 121, 10783.
- Dragt, A.J., Finn, J.M., 1976. Insolubility of trapped particle motion in a magnetic dipole field. J. Geophys. Res. 81, 2327. Dubyagin, S.V., Sergeev, V.A., Carlson, C.W., Marple, S.R., Pulkkinen, T.I., Yahnin, A.G.,
- 2003. Evidence of near-Earth breakup location. Geophys. Res. Lett. 30, 1282.
- Echim, M.M., Roth, M., de Keyser, J., 2007. Sheared magnetospheric plasma flows and discrete auroral arcs: a quasi-static coupling model. Ann. Geophys. 25, 317.
- Emery, B.A., Coumans, V., Evans, D.S., German, G.A., Greer, M.S., Holeman, E. Kadinsky-Cade, K., Rich, F.J., Xu, W., 2008. Seasonal, Kp, solar wind, and solar flux variations in long-term single-pass satellite estimates of electron and ion auroral hemispheric power. J. Geophys. Res. 113, A06311.

- Emery, B.A., Richardson, I.G., Evans, D.S., Rich, F.J., 2009. Solar wind structure sources and periodicities of auroral electron power over three solar cycles. J. Atmos. Sol. Terr. Phys. 71, 1157.
- Falthammar, C.-G., 1977. Problems related to macroscopic electric fields in the magnetosphere. Rev. Geophys. Space Sci. 15, 457.
- Feldstein, Y.I., Galperin, Y.I., 1993. An alternative interpretation of auroral precipitation and luminosity observations from the DE, DMSP, AUREOL, and Viking satellites in terms of their mapping to the nightside magnetosphere. J. Atmos. Terr. Phys. 55, 105
- Frey, H.U., Haerendel, G., Knudsen, D., Buchert, S., Bauer, O.H., 1996. Optical and radar observations of the motion of auroral arcs. J. Atmos. Sol. Terr. Phys. 58, 57.
- Galperin, Y.I., Volosevich, A.V., Zelenyi, L.M., 1992. Pressure gradient structures in the tail neutral sheet as "roots of the arcs" with some effects of stochasticity. Geophys. Res. Lett. 19, 2163.
- Galvez, M., Borovsky, J.E., 1988. The electrostatic two-stream instability driven by slabshaped and cylindrical beams injected into plasmas. Phys. Fluids 31, 857.
- Gardner, C.S., 1966. Magnetic moment to second order for axisymmetric static field. Phys. Fluids 9, 1997.
- Gilchrist, B.E., Banks, P.M., Neubert, T., Williamson, P.R., Myers, N.B., Raitt, W.J., Sasaki, S., 1990. Electron collection enhancement arising from neutral gas jets on a charged vehicle in the ionosphere. J. Geophys. Res. 95, 2469.
- Gilchrist, B.E., Khazanov, G., Krause, L., Neubert, T., 2001. Study of relativistic electron beam propagation in the atmosphere-ionosphere-magnetosphere. Tech. Rep. AFRL-VS-TR-2001-1505, Air Force Research Lab. Hanscom AFB, MA.
- Gillies, D.M., Knudsen, D.J., Donovan Spanswick, E.L., Hansen, C., Keating, D., Erion, S., 2014. A survey of quiet auroral arc orientation and the effects of the interplanetary magnetic field. J. Geophys. Res. 119, 2550.
- Gillies, D.M., Knudsen, D., Rankin, R., Milan, S., Donovan, E., 2018. A statistical survey of the 630.0-nm optical signature of periodic auroral arcs resulting from magnetospheric field line resonances. Geophys. Res. Lett. 45, 4648.
- Glukhov, V.S., Pasko, V.P., Inan, U.S., 1992. Relaxation of transient lower ionospheric disturbances caused by lightning-whistler-induced electron precipitation bursts. J. Geophys. Res. 97 (A11), 16,971.
- Goertz, C.K., 1985. Auroral arc formation: kinetic and MHD effects. Space Sci. Rev. 42, 499.
- Goertz, C.K., Boswell, R.W., 1979. Magnetosphere-ionosphere coupling. J. Geophys. Res. 84, 7239.
- Grad, H., 1964. Some new variational properties of hydromagnetic equilibria. Phys. Fluids 7, 1283.
- Habash Krause, L., Gilchrist, B.E., Neubert, T., 2000. Analysis of active space experiments using artificial relativistic electron beams. Proceedings of the 6th Spacecraft Charging Conference. AFRL-VS-TR-200001578, Hanscom AFB, USA, p. 139.
- Haerendel, G., 2007. Auroral arcs as sites of magnetic stress release. J. Geophys. Res. 112. A09214.
- Haerendel, G., 2009. Poleward arcs of the auroral oval during substorms and the inner edge of the plasma sheet. J. Geophys. Res. 114, A06214.
- Haerendel, G., 2010. Equatorward moving arcs and substorm onset. J. Geophys. Res. 115, A07212.
- Haerendel, G., 2011. Six auroral generators: a review. J. Geophys. Res. 116, A00K05. Haerendel, G., 2012. Auroral generators: a survey, Geophys. MS 197, 347.
- Haerendel, G., Buchert, S., La Hoz, C., Raaf, B., Rieger, E., 1993. On the proper motion of auroral arcs. J. Geophys. Res. 98, 6087.
- Haerendel, G., Frey, H.U., Chaston, C.C., Amm, O., Juusola, L., Nakamura, R., Seran, E., Weygand, J.M., 2012. Birth and life of auroral arcs embedded n the evening auroral oval convection: A critical comparison of observations and theory. J. Geophys. Res. 117. A12220.
- Hallinan, T.J., Winkler, J.R., Malcolm, P., Stenbaek-Nielsen, H.C., Baldridge, J., 1990. Conjugate echoes of artificially injected electron beams detected optically by means of new image processing. J. Geophys. Res. 95, 6519.
- Hasegawa, A., Sato, T., 1979. Generation of field aligned current during substorm. In:
 Akasofu, S.-I. (Ed.), Dynamics of the Magnetosphere. D. Reidel Publishing, p. 529.
- Hedin, A.E., 1987. MSIS-86 thermospheric model. J. Geophys. Res. 92, 4649. Henderson, M.G., 2012. Auroral substorms, poleward boundary activations, auroral
- streamers, omega bands, and onset precursor activity. Geophys. Monogr. 197, 39. Henderson, M.G., Donovan, E.F., Foster, J.C., Mann, I.R., Immel, T.J., Mende, S.B.,
- Henderson, M.G., Donovan, E.F., Foster, J.C., Mann, I.R., Immel, T.J., Mende, S.B., Sigwarth, J.B., 2010. Start-to-end global imaging of a sunward propagating, SAPSassociated giant undulation event. J. Geophys. Res. 115, A04210.
- Henderson, M.G., Reeves, G.D., Murphree, J.S., 1998. Are north-south aligned auroral structures an ionospheric manifestation of bursty bulk flows? Geophys. Res. Lett. 25, 3737.
- Horne, R.B., Kersten, T., Glauert, S.A., Meredith, N.P., Boscher, D., Sicard-Pier, A., 2013. Thorne RM, Li W. A new diffusion matrix for whistler mode chorus waves. J. Geophys. Res. 118, 6302.
- Hsieh, M.-S., Otto, A., 2014. The influence of magnetic flux depletion on the magnetotail and auroral morphology during the substorm growth phase. J. Geophys. Res. 119, 3430.
- Huang, C.Y., Burke, W.J., Hardy, D.A., Grough, M.P., Olsen, D.G., Gentile, L.C., Gilchrist, B.E., Bonifazi, C., Raitt, W.J., Thompson, D.C., 1998. Cerenkov emission of ion acoustic-like waves generated by electron beams emitted during TSS-1r. Geophys. Res. Lett. 23, 721.
- Il'ina, A.N., Il'in, V.D., Kuznetsov, S.N., Yushkov, B.Y., Amirkhanov, I.V., Il'in, I.V., 1993. Model of nonadiabatic charged-particle motion in the field of a magnetic dipole. J. Exp. Theor. Phys. Lett. 77, 246.
- Inan, U.S., Bell, T.F., Bortnik, J., Albert, J.M., 2003. Controlled precipitation of radiation belt electrons. J. Geophys. Res. 108, 1186.

- ITT (International Telephone and Telegraph Corporation), 1977. Reference Data for Radio Engineers. Sect. 28, Fig. 32. Howard Sams and Co., Indianapolis, Ind., pp. 26–28
- Izhovkina, N.I., JKosik, J.C., Pyatsi, A.K., Reme, H., Saint-Marc, A., Sverdlov, J.L., Uspensky, M.V., Vigo, J.M., Zarnitsky, J.F., Zhulin, I.A., 1980. Comparison between experimental and theoretical conjugate points locations in the Araks experiments. Ann. Geophys. 36, 319.
- Jones, A.W., 1974. Aurora. D. Reidel Publishing, Dordrecht.
- Karlsson, T., Andersson, L., Gillies, D.M., Lynch, K., Marghitu, O., Partamies, N., Sivadas, N., Wu, J., 2020. Quiet, discrete auroral arcs – observations. Space Sci. Rev. 216, 16.
- Katz, I., Barfield, J.N., Burch, J.L., Marshall, J.A., Gibson, W.C., Neubert, T., 1994. Interactions between the space experiments with particle plasma contactor and the ionosphere. J. Spacecraft Rockets 31, 1079.
- Kaufmann, R.L., Larson, D.J., Lu, C., 1990. Mapping and distortion of auroral structures in the quiet magnetosphere. J. Geophys. Res. 95, 7973.
- Keiling, A., Parks, G.K., Reme, H., Dandouras, I., Wilber, M., Distler, L., Owen, C., Fazakerley, A.N., Lucek, E., Maksimovic, M., Cornilleau-Wehrlin, N., 2006. Energydispersed ions in the plasma sheet boundary layer and associated phenomena: ion heating, electron acceleration, Alfvén waves, broadband waves, perpendicular electric field spikes, and auroral emissions. Ann. Geophys. 24, 2685.
- Kiraga, A., Klos, Z., Oraevsky, V., Dokukin, V., Pulinets, S., 1995. Observation of fundamental magnetoplasma emissions excited in magnetosphere by modulated electron beams. Adv. Space Res. 15 (12), 21.
- Knudsen, D.J., 1996. Spatial modulation of electron energy and density by nonlinear stationary inertial Alfvén waves. J. Geophys. Res. 101, 10761.
- Knudsen, D.J., Donovan, E.F., Cogger, L.L., Jackel, B., Shaw, W.D., 2001. Width and structure of mesoscale optical auroral arcs. Geophys. Res. Lett. 28, 705.
- Kozlovsky, A., Lakkala, T., Kangas, J., Aikio, A., 2001. Response of the quiet auroral arc motion to ionospheric convection variations. J. Geophys. Res. 106, 21463.
- Krause, L.H., 1998. The Interaction of Relativistic Electron Beams with the Near-Earth Space Environment, PhD Thesis. Univ. of Michigan, Ann Arbor, Michigan.
- Kremser, G., Korth, A., Ullaland, S.L., Perraut, S., Roux, A., Pedersen, A., Schmidt, R., Tanskanen, P., 1988. Field-aligned beams of energetic electrons (16 keV < E < 80 keV) observed at geosynchronous orbit at substorm onset. J. Geophys. Res. 93, 14453.
- Lanchester, B., 2017. Some remaining mysteries in the aurora. Astron. Geophys. 58, 3–17.
- Langmuir, I., Blodget, K.B., 1924. Current limited by space charge between concentric spheres. Phys. Rev. 23, 49.
- Lavergnat, J., 1982. The French-Soviet experiment ARAKS: main results. In: Grandal, B. (Ed.), Artificial Particle Beams in Space Plasma Studies. Plenum, New York pg. 87.
- Lehtinen, N.G., Inan, U.S., 2007. Possible persistent ionization caused by giant blue jets. Geophys. Res. Lett. 34, L08804.
- Lessard, M.R., Lotko, W., LaBelle, J., Peria, W., Carlson, C.W., Creutzberg, F., Wallis, D. D., 2007. Ground and satellite observations of the evolution of growth phase auroral arcs. J. Geophys. Res. 112, A09304.
- Lewellen, J.W., Buechler, C.B., Carlsten, B.F., Dale, G.E., Holloway, M.A., Patrick, D., Storms, S.A., Nguyen, D.C., 2019. Space borne electron accelerator design. Front. Astron. Space Sci. 6, 35.
- Lorentzen, K.R., Looper, M.D., Blake, J.B., 2001. Relativistic electron microbursts during the GEM storms. Geophys. Res. Lett. 28, 2573.
- Lu, G., Brittnacher, M., Parks, G., Lummerzheim, D., 2000. On the magnetospheric source regions of substorm-related field-aligned currents and auroral precipitation. J. Geophys. Res. 105, 18483.
- Lucco Castello, F., Delzanno, G.L., Borovsky, J.E., Miars, G., Leon, O., Gilchrist, B.E., 2018. Spacecraft-charging mitigation of a high-power electron beam emitted by a magnetospheric spacecraft: simple theoretical model for the transient of the spacecraft potential. J. Geophys. Res. 123, 6424.
- Marklund, G., 1984. Auroral arc classification scheme based on the observed areassociated electric field pattern. Planet. Space Sci. 32, 193.
- Marklund, G., Sandahl, I., Opgenoorth, H., 1982. A study of the dynamics of a discrete auroral arc. Planet. Space Sci. 30, 179.
- Marshall, R.A., Nicolls, M., Sanchez, E., Lehtinen, N.G., Neilson, J., 2014. Diagnostics of an artificial relativistic electron beam interacting with the atmosphere. J. Geophys. Res. 119, 8560.
- Marshall, R.A., Xu, W., Kero, A., Kabirzadeh, R., Sanchez, E., 2019. Atmospheric effects of a relativistic electron beam injected from above: chemistry, electrodynamics, and radio scattering. Front. Astron. Space Sci. 6, 6.
- Mauk, B.H., Meng, C.-I., 1991. The aurora and middle magnetospheric processes. In: Meng, C.-I., Rycroft, M.J., Frank, L.A. (Eds.), Auroral Physics. Cambridge Press, Cambridge, p. 223.
- McIlwain, C.E., 1975. Auroral electron beams near the magnetic equator. In: Hultqvist, B., Stenflo, L. (Eds.), Physics of the Hot Plasma in the Magnetosphere. Plenum, New York, p. 91.
- McNutt, R.L., Rieder, R.J., Keneshea, T.J., LePage, A.J., Rappaport, S.A., Pualsen, D.E., 1995. Energy deposition in the upper atmosphere in the EXCEDE III experiment. Adv. Space Res. 15 (12), 13.
- Mende, S.B., 2016a. Observing the magnetosphere through global auroral imaging: 1. Observables. J. Geophys. Res. 121, 10623.
- Mende, S.B., 2016b. Observing the magnetosphere through global auroral imaging: 2. Observing techniques. J. Geophys. Res. 121, 10638.
- Meng, C.-I., Mauk, B., McIlwain, C.E., 1979. Electron precipitation of evening diffuse aurora and its conjugate electron fluxes near the magnetospheric equator. J. Geophys. Res. 84, 2545.

- Miars, G., Leon, O., Gilchrist, B.E., Delzanno, G.L., Borovsky, J.E., 2016. Electrically Isolated System Response to Rapid Charging Events Using Hollow Cathode Neutralization, 14th Spacecraft Charging Technology Conference. Noordwijk, Netherlands. April 4-8.
- Miars, G., Leon, O., Gilchrist, B.E., Delzanno, G.L., Lucco Castello, F., Borovsky, J.E., 2017. Ion Emission Experiments Enabling Electron Beam Emission in Tenuous Plasmas. Active Experiments in Space, pp. 11–15. Santa Fe, NM, September.
- Miars, G., Leon, O., Gilchrist, B.E., Delzanno, G.L., Lucco Castello, F., 2018a. Parametric Experiments in Mitigating Spacecraft Charging via Plasma Contactor. American Geophysical Union Fall Meeting, Washington D.C., USA, December, pp. 10–14.
- Miars, G., Delzanno, G.L., Lucco Castello, F., Leon, O., Gilchrist, B.E., 2018b. Enabling Electron Beam Use in Tenuous Space Plasmas Using Plasma Contactors: the Ion Emission Model, 15th Spacecraft Charging Technology Conference. Kobe, Japan. June 25-29.
- Miars, G., Delzanno, G.L., Gilchrist, B.E., Leon, O., Lucco Castello, F., Borovsky, J.E., 2020. Ion emission from a positively biased hollow cathode plasma. IEEE Transactions of Plasma Science submitted for publication.
- Motoba, T., Ohtani, S., Anderson, B.J., Korth, H., Mitchell, D., Lanzerotti, L., Shiokawa, K., Connors, M., Kletzing, C.A., Reeves, G.D., 2015. On the formation and origin of substorm growth phase/onset auroral arcs inferred from conjugate spaceground observations. J. Geophys. Res. 120, 8707.
- Mott-Smith, H., Langmuir, I., 1926. The theory of collectors in gaseous discharges. Phys. Rev. 28, 727.
- Mourenas, D., Zhang, X.J., Artemyev, A.V., Angelopoulos, V., Thorne, R.M., Bortnik, J., et al., 2018. Electron nonlinear resonant interaction with short and intense parallel chorus wave packets. J. Geophys. Res. Space Phys. 123, 4979.
- Mozer, F.S., 1966. Proton trajectories in the radiation belt. J. Geophys. Res. 71, 2701.
 NASA, 2003. Sun-Earth Connection Roadmap 2003-2028 pg. 92. http://www.dept.aoe.
 vt.edu/~cdhall/courses/aoe4065/NASADesignSPs/SEC 2003 roadmap full.pdf.
- NASA, 2006. Heliophysics: the New Science of the Sun-Solar System Connection:
 Recommended Roadmap for Science and Technology 2005-2035. National
 Aereonautics and Space Administration, Washington, DC.
- National Research Council, 2012. Magnetosphere-to-ionosphere field-line tracing technology. Solar and Space Physics: A Science for a Technological Society. National Academies Press, Washington, D. C, p. 333.
- Neubert, T., Gilchrist, B.E., 2002. Particle simulations of relativistic electron beam injection from spacecraft. J. Geophys. Res. 107, 1167.
- Neubert, T., Gilchrist, B.E., 2004. Particle simulations of relativistic electron beam injection from spacecraft: performance and applications. Adv. Space Res. 34, 2409.
- Neubert, T., Taylor, W.W.L., Storey, L.R.O., Kawashima, N., Roberts, W.T., Reasoner, D. L., Burch, J.L., 1986. Waves generated during electron beam emissions from the space shuttle. J. Geophys. Res. Space Phys. 91, 11321.
- Neubert, T., Banks, P.M., Gilchrist, B.E., Fraser-Smith, A.C., Williamson, P.R., Raitt, W.J., Myers, N.B., Sasaki, S., 1990. The interaction of an artificial electron beam with the Earth's upper atmosphere: effects on spacecraft charging and the near-plasma environment. J. Geophys. Res. 95, 12209.
- Neubert, T., Gilchrist, B., Wilderman, S., Habash, L., Wang, H.J., 1996. Relativistic electron beam propagation in the earth's atmosphere: modeling results. Geophys. Res. Lett. 23, 1009.
- Newell, P.T., Sotirelis, T., Wing, S., 2009. Diffuse, monoenergetic, and broadband aurora: the global precipitation budget. J. Geophys. Res. 114, A09207.
- Ni, B., Thorne, R.M., Zhang, X.J., Bortnik, J., Pu, A., Xie, L., Hu, Z.J., Han, D., Shi, R., Zhou, C., Gu, X., 2016. Origins of the Earth's diffuse auroral precipitation. Space Sci. Rev. 200. 205.
- Nishimura, Y., Bortnik, J., Li, W., Thorne, R.M., Lyons, L.R., Angelopoulos, V., Mende, S. B., Bonnell, J., Le Contel, O., Cully, C., Ergun, R., Auster, U., 2011. Estimation of magnetic field mapping accuracy using the pulsating aurora-chorus connection. Geophys. Res. Lett. 38. L14110.
- Nishimura, Y., Lessard, M.R., Katoh, Y., Miyoshi, Y., Grono, E., Partamies, N., Sivadas, N., Hosokawa, K., Fukizawa, M., Samara, M., Michell, R.G., Kataoka, R., Sakanoi, T., Whiter, D.K., Oyama, S.-I., Ogawa, Y., Kurita, S., 2020. Diffuse and pulsating aurora. Space Sci. Rev. 216, 4.
- Northrop, T.G., 1963. The Adiabatic Motion of Charged Particles. John Wiley, New York. Nunz, G.J., 1990. Beam experiments aboard a rocket (BEAR) project final report. In: Project Summary, Los Alamos National Laboratory Report LA-11737-MS, vol. 1 (Los Alamos, New Mexico).
- Ober, D.M., Maynard, N.C., Burke, W.J., Moen, J., Egeland, A., Sandhold, P.E., Farrugia, C.J., Weber, E.J., Scudder, J.D., 2000. Mapping prenoon auroral structures to the magnetosphere. J. Geophys. Res. 105, 27519.
- Olsen, R.C., 1985. Experiments in charge control at geosynchronous orbit—ATS-5 and ATS-6. J. Spacecraft Rockets 22, 254.
- Omholt, A., 1971. The Optical Aurora. Sect. 2.2. Springer-Verlag, New York.
- Omura, Y., et al., 2015. Formation process of relativistic electron flux through interaction with chorus emissions in the Earth's inner magnetosphere. J. Geophys. Res. Space Phys. 120, 9545.
- Ono, T., Ejiri, M., Hirasawa, T., Kaya, N., Mukai, T., 1987. A case study of an active aurora observed by monocromatic auroral TV on the ground and particle analyzers on board the EXOS-C satellite. J. Geomagn. Geoelectr. 39, 119.
- Opgenoorth, H.J., Haggstrom, I., Williams, P.J.S., Jones, G.O.L., 1990. Regions of strongly enhanced perpendicular electric fields adjacent to auroral arcs. J. Atmos Terr. Phys. 52, 449.
- Orlova, K.G., Shprits, Y., Ni, B., 2012. Bounce-averaged diffusion coefficients due to resonant ingteraction of the outer radiation belt electrons with oblique chorus waves computed in a realistic magnetic field model. J. Geophys. Res. 117, A07209.

- O'Neil, R.R., Shepherd, O., Reidy, W.P., Carpenter, J.W., Davis, T.N., Newell, D., Ulwick, J.C., Stair, A.T., 1978. Excede 2 test, an artificial auroral experiment: ground-based optical measurements. J. Geophys. Res. 83, 3281
- O'Shea, P.G., Butler, T.A., Lynch, M.T., McKenna, K.F., Pongratz, M.B., Zaugg, T.J., 1991.

 A linear accelerator in space the beam experiment aboard rocket. Proceedings of the 1990 Linear Accelerator Conference. Los Alamos National Laboratory, Los Alamos, New Mexico pg. 739-742.
- Partamies, P., Syrjasuo, M., Donovan, E., Conners, M., Charrois, D., Knudsen, D., Kryzanowsky, Z., 2010. Observations of the auroral width spectrum at kilometerscale size. Ann. Geophys. 29, 711.
- Partamies, N., Bolmgren, K., Heino, E., Ivchenko, N., Gustavsson, B., Borovsky, J.E., Dahlgren, H., 2019. Patch size evolution during pulsating aurora. J. Geophys. Res. 124, 4725.
- Paschmann, G., Melzner, F., Frenzel, R., Vaith, H., Parigger, P., Pagel, U., Bauer, O.H., Haerendel, G., Baumjohann, W., Scopke, N., Torbert, R.B., Briggs, B., Chan, J., Lynch, K., Morey, K., Quinn, J.M., Simpson, D., Young, C., McIlwain, C.E., Fillius, W., Kerrm, S.S., Mahieu, R., Whipple, E.C., 1998. The electron drift instrument for cluster. Space Sci. Rev. 79, 233.
- Paschmann, G., Haaland, S., Treumann, R., 2002. Auroral plasma physics. Space Sci. Rev. 104. 1–4.
- Pellat, R., Sagdeev, R.Z., 1980. Concluding remarks on the ARAKS experiments. Ann. Geophys. 36, 443.
- Penndorf, R., 1957. Tables of the refractive index for standard air and the Rayleigh scattering coefficient for the spectral region between 0.2 and 20.0 μ and their application to atmospheric optics. J. Optical Soc. Amer. 47, 176.
- Pongratz, M.B., 2018. History of Los Alamos participation in active experiments in space. Front Physics 6, 144.
- Porazik, P., Johnson, J.R., Kaganovich, I., Sanchez, E., 2014. Modification of the loss cone for energetic particles. Geophys. Res. Lett. 41, 8107.
- Prech, L., Nemecek, Z., Safrankova, J., Simunek, J., Truhlik, V., Shutte, N.M., 1995.
 Response of the electron energy distribution to an artificially emitted electron beam:
 APEX experiment. Adv. Space Res. 15 (12), 33.
- Prech, L., Ruzhin, Y.Y., Dokukin, V.S., Nemecek, Z., Safrankova, J., 2018. Overview of APEX project results. Front. Astron. Space Sci. 5, 46.
- Pulkkinen, T.I., Koskinen, H.E.J., Pellinen, R.J., 1991. Mapping of auroral arcs during substorm growth phase. J. Geophys. Res. 96, 21087.
- Raitt, W.J., White, A.B., Fraser-Smith, A.C., Gilchrist, B.E., Hallinan, T.J., 1995. VLF wave experiments in space using a modulated electron beam. J. Spacecraft Rockets 32, 670.
- Rappaport, S.A., Rieder, R.J., Reidy, W.P., McNutt, R.L., Atkinson, J.J., Paulsen, D.E., 1993. Remote x-ray measurements of the electron-beam from the EXCEDE-III experiment. J. Geophys. Res. 98, 19093.
- Rees, M.H., 1963. Auroral ionization and excitation by incident energetic electrons, Planet. Space Sci 11, 1209.
- Reeves, G.D., Banks, P.M., Neubert, T., Harker, K.J., Gurnett, D.A., 1990. VLF wave emissions by pulsed and DC electron beams in space: 2. Analysis of Spacelab 2 results. J. Geophys. Res. 95, 6505.
- Reeves, G., Delzanno, G.L., Fernandez, P., Yakymenko, K., Carlsten, B., Lewellen, J., Holloway, M., Nguyen, D., Pfaff, R., Farrel, B., Rowland, D., Samara, M., Sanchez, E., Spanswick, E., Donovan, E., Roytershteyn, V., 2020. The Beam Plasma Interactions Experiment: an Active Experiment Using Pulsed Electron Beams. Los Alamos National Laboratory Unclassified Report, LAUR, Los Alamos, New Mexico.
- Rinnert, K., Kohl, H., Schlegel, K., Wilhelm, K., 1986. Electric field configuration and plasma parameters in the vicinity of a faint auroral arc. J. Atmos. Terr. Phys. 48, 867.
- Rodger, C.J., Clilverd, M.A., Dowden, R.L., 2002. D region reflection height modification by whistler-induced electron precipitation. J. Geophys. Res. 107, 1145.
- Rodger, C.J., Nunn, D., Clilverd, M.A., 2004. Investigating radiation belt losses through numerical modeling of precipitating fluxes. Ann. Geophys. 22, 3657.
- Rodger, C.J., Enell, C.F., Turunen, E., Clilverd, M.A., Thomson, N.R., Verronen, P.T., 2007. Lightning-driven inner radiation belt energy deposition into the atmosphere: implications for ionisation-levels and neutral chemistry. Ann. Geophys. 25, 1745.
- Rossi, B., Olbert, S., 1970. Introduction to the Physics of Space. McGraw-Hill. Roth, M., Evans, D.S., Lemaire, J., 1993. Theoretical structure of a magnetospheric
- Roth, M., Evans, D.S., Lemaire, J., 1993. Theoretical structure of a magnetospheric plasma boundary: application to the formation of discrete auroral arcs. J. Geophys. Res. 98, 11411.
- Safargaleev, V.V., Kozlovsky, A.E., Osipenko, S.V., Tagirov, V.R., 2003. Azimuthal expansion of high-latitude auroral arcs. Ann. Geophys. 21, 1793.
- Samson, J.C., Gogger, L.L., Pao, Q., 1996. Observations of field line resonances, auroral arcs, and auroral vortex structures. J. Geophys. Res. 101, 17373.
- Sanchez, E.R., Powis, A.T., Kagonovich, I.D., Marshall, R., Porazik, P., Johnson, J., Grekiek-Mckeon, M., Amin, K.S., Shaw, D., Nicolls, M., 2019. Relativistic particle beams as a resournce to solve outstanding problems in space physics. Front. Astron. Space Sci. 6, 71.
- Sandahl, I., Brandstrom, U., Sergienko, T., 2011. Fine structure of aurora. Int. J. Rem. Sens. 32, 2947.
- Sangalli, L., Gustovsson, B., Partamies, N., Kauristie, K., 2011. Calculating the peak auroral emission altitude from all-sky images. Opt. Pura Apl. 44, 593.
- Sato, T., 1978. A theory of quiet auroral arcs. J. Geophys. Res. 83, 1042.
- Sato, T., Iijima, T., 1979. Primary sources of large-scale Birkeland currents. Space Sci. Rev. 24, 347.
- Schindler, K., Birn, J., 1978. Magnetospheric physics. Phys. Rep. 47, 109.
- Schindler, K., Birn, J., 2002. Models of two-dimensional embedded thin current sheets from Vlasov theory. J. Geophys. Res. 107, SMP20.
- Schneider, B.I., Brau, C.A., 1982. Two- and three-body electron attachment in air. J. Phys. B Atom. Mol. Phys. 15, 1601.

- Sergeev, V.A., Sazhina, E.M., Tsyganenko, N.A., Lundblad, J.A., Sorras, F., 1983. Pitch-angle scattering of energetic protons in the magnetotail current sheet as the dominant source of their isotropic precipitation into the nightside ionosphere. Planet. Space Sci. 31, 1147.
- Sergeev, V., Nishimura, Y., Kubyshkina, M., Angelopoulos, V., Nakamura, R., Singer, H., 2012. Magnetospheric location of the equatorial pregreakup arc. J. Geophys. Res. 117, A01212.
- Shevchenko, I.G., Sergeev, V., Kubyshkina, M., Angelopoulos, V., Glassmeier, K.H., Singer, H.J., 2010. Estimation of magnetosphere-ionosphere mapping accuracy using isotropy boundary and THEMIS observations. J. Geophys. Res. 115, A11206.
- Shiokawa, K., Baumjohann, W., Haerendel, G., 1997. Braking of high-speed flows in the near-Earth tail. Geophys. Res. Lett. 24, 1179.
- Sitnov, M.I., Tsyganenko, N.A., Ukhorskiy, A.Y., Brandt, P.C., 2008. Dynamical data-based modeling of the storm-time geomagnetic field with enhanced spatial resolution. J. Geophys. Res. 113, A07218.
- Spanswick, E., Donovan, E., Liang, J., Weatherwax, A.T., Skone, S., Hampton, D.L., Gillies, M., Yang, B., Chaddock, D., Vollmerhaus, L., Kujawski, J.T., 2018. First-Light Observations from the Transition Region Explorer (TREx) Ground-Based Network. American Geophysical Union, Fall Meeting abstract SM23B-04,2018AGUFMSM23B.
- Spjeldvik, W.N., Rothwell, P.J., 1985. In: Jursa, A.S. (Ed.), The Radiation Belts, Handbook of Geophysics and the Space Environment. National Technical Information Service, Springfield, Virginia, pp. 5–7.
- Stasiewicz, K., 1985. Generation of magnetic-field aligned currents, parallel electric field, and inverted-V structures by plasma pressure inhomogeneities in the magnetosphere. Planet. Space Sci. 9, 1037.
- Steele, D.P., McEwen, D.J., 1990. Electron auroral excitation efficiencies and intensity ratios. J. Geophys. Res. 95, 10321.
- Stenbaek-Nielsen, H.C., Hallinan, T.J., Osborne, D.L., Kimball, J., Chaston, C., McFadden, J., Delory, G., Temerin, M., Carlson, C.W., 1998a. Aircraft observations conjugate to FAST: auroral arc thicknesses. Geophys. Res. Lett. 2, 2073.
- Stenbaek-Nielsen, H.C., Hallinan, T.J., Osborne, D.L., Kimball, J., 1998b. Aircraft observations conjugate to FAST: auroral arc thicknesses. Geophys. Res. Lett. 25, 2073
- Strangeway, R.J., 2012. The relationship between magnetospheric processes and auroral field-aligned current morphology. Geophys. Monogr. 197, 355.
- Swift, D.W., 1978. Mechanisms for the discrete aurora A review. Space Sci. Rev. 22, 35.
 Thomsen, M.F., McComas, D.J., Reeves, G.D., Weiss, L.A., 1996. An observational test of the Tsyganenko (T89a) model of the magnetospheric field. J. Geophys. Res. 101, 24827
- Thomsen, M.F., McComas, D.J., Borovsky, J.E., Elphic, R.C., 1998. The magnetospheric trough. Geophys. Mong. Ser. 104, 355.
- Thomsen, M.F., Henderson, M.G., Jordanova, V.K., 2013. Statistical properties of the surface-charging environment at geosynchronous orbit. Space Weath 11, 237.
- Thorne, R.M., Ni, B., Horne, R.B., Meredith, N.P., 2010. Scattering by chorus waves as the dominant cause of diffuse auroral precipitation. Nature 467, 943.
- Torbert, R.B., Russell, C.T., Magnes, W., Ergun, R.E., Lindqvist, P.-A., LeContel, O., Vaith, H., Macri, J., Myers, S., Rau, D., et al., 2014. He FIELDS instrument suite on MMS: scientific objectives, measurements, and data products. Space Sci. Rev. 199, 195.
- Torbert, R.B., Vaith, H., Granoff, M., Widholm, M., Gaidos, J.A., Briggs, B.H., Dors, I.G., Chutter, M.W., Macri, J., Argall, M., Bodet, D., Needell, J., Steller, M.B., Baumjohann, W., Nakamura, R., Plaschke, F., Ottacher, H., Hasiba, J., Hofmann, K., Kletzing, C.A., 2016. Bounds, SR, dvorsky, RT, sigsbee, K, kooi, V., the electron drift instrument for MMS. Space Sci. Rev. 199, 283.
- Trondsen, T.S., Cogger, L.L., 1997. High-resolution television observations of black aurora. J. Geophys. Res. 102, 363.
- Tsyganenko, N.A., 1989. A magnetospheric magnetic field model with a warped tail current sheet, Planet. Space Sci 37, 5.

- Tsyganenko, N.A., Sitnov, M.I., 2007. Magnetospheric configurations from a high-resolution data-based magnetic field model. J. Geophys. Res. 112, A06225.
- Tsyganenko, N.A., Usmanov, A.V., 1982. Determination of the magnetospheric current system parameters and development of experimental field models based on data from IMP and HEOS satellites, Planet. Space Sci 30, 985.
- Usanova, M.E., Mann, I.R., Bortnik, J., Shao, L., Angelopoulos, V., 2012. THEMIS observations of electromagnetic ion cyclotron wave occurrence: dependence on AE, SYMH, and solar wind dynamic pressure. J. Geophys. Res. 117, A10218.
- Uspensky, M.V., Timopheev, E.E., Sverdlov, Y.L., 1980. "Araks" Doppler radar measurements of the ionospheric effects of artificial electron beam in the North hemisphere. Ann. Geophys. 36, 303.
- Vasyliunas, V.M., 1970. Mathematical models of magnetospheric convection and its coupling to the ionosphere. In: McCormac, B.M. (Ed.), Particles and Fields in the Magnetosphere. D. Reidel, Dordrecht, Holland, pp. 60–71.
- Verronen, P.T., Andersson, M.E., Rodger, C.F., Clilverd, M.A., Wang, S., Turunen, E., 2013. Comparison of modeled and observed effects of radiation belt electron precipitation on mesospheric hydroxyl and ozone. J. Geophys. Res. 118, 11419.
- Vickrey, J.F., Vondrak, R., Matthews, J., 1982. Energy deposition by precipitating particles and Joule dissipation in the auroral ionosphere. J. Geophys. Res. 87, 5184.
- Wagner, K.H., 1971. Ionization, electron-attachment, -detachment, and charge-transfer in oxygen and air. Z. Phys. 241, 258.
- Watanabe, T.-H., 2014. A unified model of auroral arc growth and electron acceleration in the magnetosphere-ionosphere coupling. Geophys. Res. Lett. 41, 6071.
- Weiss, L.A., Thomsen, M.F., Reeves, G.D., McComas, D.J., 1997. An examination of the Tsyganenko (T89A) field model using a database of two-satellite magnetic conjunctions. J. Geophys. Res. 102, 4911.
- Willard, J.M., Johnson, J.R., Snelling, J.M., Powis, a.T., Kaganovich, I.D., Sanchez, E.R., 2019a. Effect of field-line curvature on the ionospheric accessibility of relativistic electron beam experiments. Front. Astron. Space Sci. 6, 56.
- Willard, J.M., Johnson, J.R., Snelling, J.M., Powis, a.T., Kaganovich, I.D., Sanchez, E.R., 2019b. Methods for approximating field-line curves using ionospheric observations of energy-variable electron beams launched from satellites. Front. Astron. Space Sci. 6, 59.
- Williams, P.J.S., del Pozo, C.F., Hiscock, I., Fallows, R., 1998. Velocity of auroral arcs drifting equatorward from the polar cap. Ann. Geophys. 16, 1322.
- Winckler, J.R., 1992. Controlled experiments in the Earth's magnetosphere with artificial electron beams. Rev. Mod. Phys. 64, 859.
- Winckler, J.R., Arnoldy, R.L., Hendrickson, R.A., 1975. Echo-2: study of electron beams injected into the high latitude ionosphere from a large sounding rocket. J. Geophys. Res. 80, 2083.
- Wu, J., Knudsen, D.J., Gilles, D.M., Donovan, E.F., Burchill, J.K., 2017. Swarm observation of field-aligned currents associated with multiple auroral arc systems. J. Geophys. Res. 122, 10145.
- Yahnin, A.G., Yahnina, T.A., 2007. Energetic proton precipitation related to ioncyclotron waves. J. Atmos. Sol. Terr. Phys. 69, 1690.
- cyclotron waves. J. Atmos. Sol. Terr. Phys. 69, 1690.

 Yahnin, A.G., Sergeev, V.A., Gvozdevsky, B.B., Vennerstrom, S., 1997. Magnetospheric source region of discrete auroras inferred from their relationship with isotropy boundaries of energetic particles. Ann. Geophys. 15, 943.
- Yahnin, A.G., Sergeev, V.A., Gvozdevsky, B.B., Vennerstrom, S., 1999. Reply. Ann. Geophys. 17, 42.
- Yang, J., Wolf, R.A., Toffoletto, F.R., Sazykin, S., 2013. RCM-E simulation of substorm growth phase arc associated with large-scale adiabatic convection. Geophys. Res. Lett. 40, 6017
- Young, S.L., Denton, R.E., Anderson, B.J., Hudson, M.K., 2008. Magnetic field line curvature induced pitch angle diffusion in the inner magnetosphere. J. Geophys. Res. 113, A03210
- Zhulin, I.A., Kustov, A.V., Uspensky, M.V., Miroshnikova, 1980. TV, Radar observations of the overdense ionospheric ionization created by the artificial electron beam in the "Zarnitza-2" experiment. Ann. Geophys. 36, 313.